7-21-2008

InAs/Ga(In)Sb superlattice based infrared detectors using nBn design

Greg Bishop

Greg Bishop
Candidate

Electrical and Computer Engineering
Department

This thesis is approved, and it is acceptable in quality and form for publication on microfilm:

Approved by the Thesis Committee:

, Chairperson

Accepted:

Dean, Graduate School

Date

InAs/Ga(In)Sb Superlattice Based Infrared Detectors using nBn Design

by

Greg Bishop

B. S., Electrical and Computer Engineering,
University of New Mexico, 2006

THESIS

Submitted in Partial Fulfillment of the
Requirements for the Degree of

Master of Science
Electrical Engineering

The University of New Mexico
Albuquerque, New Mexico

May, 2008

Acknowledgements

I would like to acknowledge my advisor Prof. Sanjay Krishna for encouraging me to attend graduate school and for help and guidance throughout the course of this work. I would also like to thank my thesis committee, Prof. Luke Lester and Prof. Ralph Dawson for their help and questions during the defense and with the manuscript. I am eternally grateful to Dr. Elena Plis for proofreading my manuscript and the incredible boost that it provided to the overall structure, readability and flow of my thesis. I would ask like to acknowledge the group members who contributed to this work either in growth or processing of samples both of which I did not do myself, Dr. J.B. Rodriguez, Dr. Elena Plis, Dr. Yagya Sharma, Ha Sul Kim and Arezou Khoshakhalagh.

I would like to thank my family and friends for support and understanding. I would especially like to thank my wife, Kelli for sacrificing so much so that I could finish this degree.

InAs/Ga(In)Sb Superlattice Based Infrared Detectors using nBn Design

by

Greg Bishop

ABSTRACT OF THESIS

Submitted in Partial Fulfillment of the
Requirements for the Degree of

Master of Science
Electrical Engineering

The University of New Mexico
Albuquerque, New Mexico

May, 2008

InAs/Ga(In)Sb Superlattice Based Infrared Detectors using nBn Design

by

Greg Bishop

B.S., Electrical and Computer Engineering, University of New Mexico, 2006

M.S., Electrical Engineering, University of New Mexico, 2008

Abstract

Infrared detectors in the mid-wave infrared (MWIR) (3-5μm) and long-wave infrared (LWIR) (8-12μm) have many applications in military, industrial and medical fields. The state-of-the-art photodetectors based on $Hg_{1-x}Cd_xTe$ (MCT) have large signal over noise ratio and their bandgap can be tuned to span 1-32 μm wavelength range. However, large tunneling and Auger dark currents due to low electron effective mass in MCT detectors require operation at cryogenic temperatures (77-100 K). The cooling requirement limits the lifetime, adds weight and expense and increases the power consumption of the infrared system. There is a concerted effort to develop photonic detectors operating at higher temperatures. InAs/GaSb strained layer superlattice (SLS) photodectors are now considered as a promising technology for both MWIR and LWIR wavelength ranges. The bandgap of the SLS can be adjusted by controlling the thickness of the constituent InAs and GaSb layers during the growth process. InAs/GaSb SLS can also span the 3-30

μm wavelength range. Moreover, the large splitting of the energy levels of the different valence subbands in SLS contribute to the suppression of Auger recombination.

The recently proposed nBn heterostructure design has demonstrated a 100 K increase in background-limited infrared photodetection (BLIP) for InAs-based device, by decreasing Shockley-Read-Hall generation currents and by suppressing surface currents using specific processing.

This work is focused on combining the nBn detector design with InAs/GaSb superlattice material utilizing an AlGaSb barrier layer to improve detector performance and to increase the operating temperature of Focal Plane Arrays. This thesis covers three topics: Optical and electrical characteristics of single pixel devices in both the MWIR and LWIR, the reduction of surface leakage currents by using a shallow isolation etch for definition of the top contact mesa and comparison between nBn detector and PIN LWIR detectors.

List of Figures

List of Tables

1 Introduction

1.1 Electromagnetic Spectrum

The photon is the elementary particle of light. Everything with temperature above absolute zero (0K) gives off photons. The electromagnetic (EM) spectrum classifies the entire range of possible photon energy. The different regions of the EM spectrum have been given different names according to their frequency or corresponding wavelength, as shown in figure 1.1.

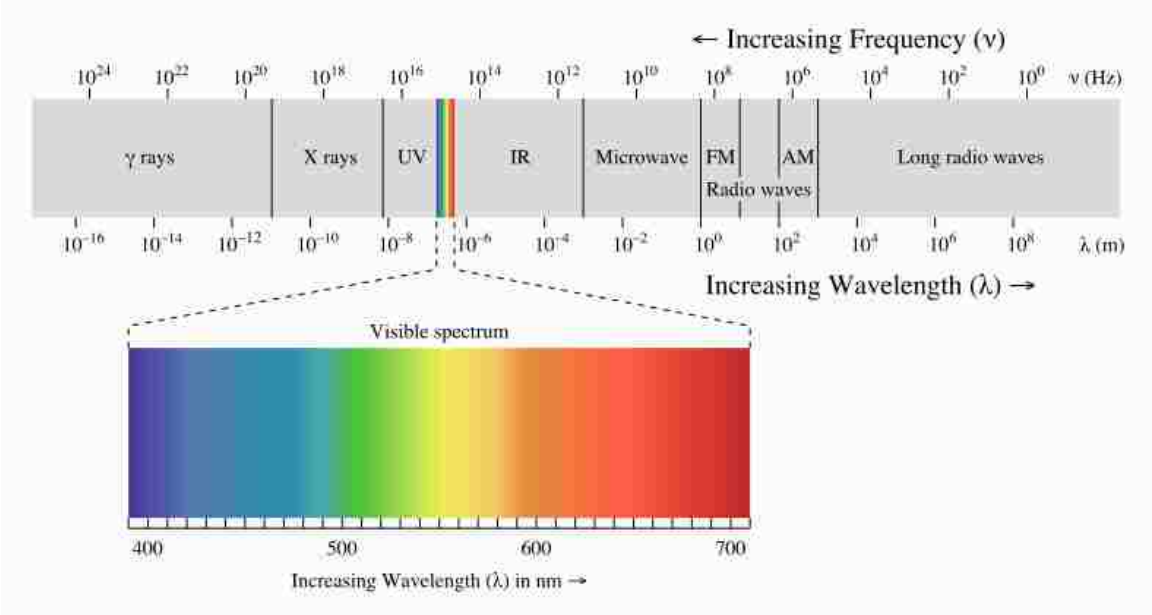

Figure 1.1 The Electromagnetic Spectrum[1]

The emitting properties of an object depends on its temperature, material, and surface condition. Blackbody (BB) is a convenient construct for the study of emmitance of radiation of an object at given temperature since the emitted radiation depends only on the temperature of the blackbody. BB is a hypothetical entity that absorbs all EM

radiation that is incident on it and transmits or reflects none and emits energy with perfect efficiency.

In 1900, Max Planck created an equation for the emission of radiation of a blackbody that matched the measured values. This equation, known as Planck's law[2,3], is

$$M_e(\lambda,T) = \frac{2\pi hc^2}{\lambda^5(e^{\frac{hc}{\lambda kT}} - 1)} \tag{1.1}$$

where k is Boltzmann's constant, h is Planck's constant and c is the speed of light where the units are W/(cm^2·μm) defines a probability distribution of blackbody radiation at a given temperature and is shown in Figure 1.2. The idea behind Plank's law was the presupposition of a relationship between photon energy E and photon frequency υ and frequency of EM radiation in vacuum. Planck assumed that E is proportional to the oscillation frequency υ giving

$$E = h\upsilon = h\frac{c}{\lambda} \tag{1.2}$$

Two more important laws that give more information about blackbody radiation are Wien's law and the Stefan-Boltzmann law. Wien's law gives the peak of the distribution of EM energy emitted by BB at a given temperature and is given by

$$\lambda_{\max} = \frac{2898}{T} \tag{1.3}$$

where T is in Kelvin and λ_{max} is in microns. The Stefan-Boltzmann law estimates the total energy radiated by a blackbody at a given temperature and is given by

$$M = \sigma T^4 \tag{1.4}$$

where σ is the Stefan-Boltzmann constant given by[4]

$$\sigma = \frac{2\pi^5 k^4}{15c^2 h^3} = 5.7604x10^{-8} \frac{W}{cm^2 K^4} \tag{1.5}$$

From Wien's law, which is represented by the dashed line in Figure 1.2, one can see that with increasing BB temperature the peak of Planck's function moves to the shorter wavelengths.

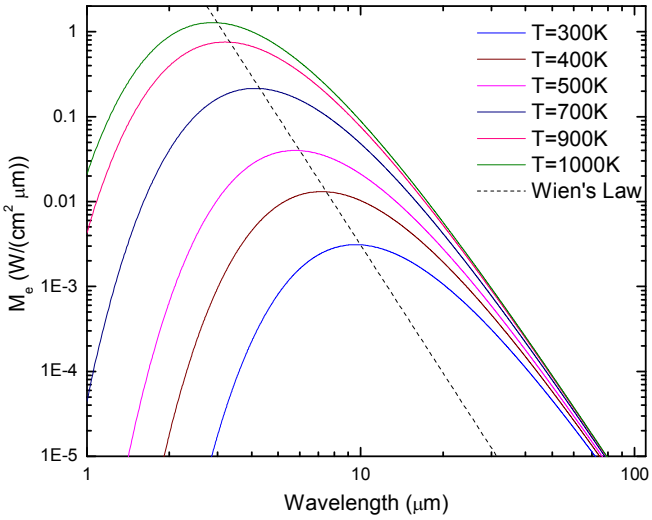

Figure 1.2 Planck's Law: spectral exitance vs. wavelength for BB temperature ranging from 300 K to 1000 K. Dashed line represents Wien's Law.

All of the laws related to the idealized blackbody are applicable to the real objects by introducing a parameter called emissivity. It is defined as the ratio between the exitance of the actual object and the exitance of the BB. The emissivity of an ideal blackbody is one while laboratory blackbodies can be within a few percent of unity.

The peak wavelength of emission spectrum of the sun (6000 K) corresponds to 0.5 μm which is in the middle of the visible spectrum. For objects at or around ambient temperature (300 K) including humans, the peak wavelength of emission spectrum is

close to 10 μm. This wavelength falls in the infrared (IR) part of the EM spectrum and can be detected as heat.

1.2 Infrared radiation

Infrared or thermal radiation has been defined as the part of the EM spectrum with wavelength longer than visible light and shorter than radio waves. By convention, the range of the infrared spectrum is from ~0.7 μm to 1000 μm. Different molecules in the atmosphere absorb different wavelengths of infrared radiation as shown in Figure 1.3. Water vapor absorbs infrared radiation from 5.5 μm to 7.5 μm and for various wavelengths from 0.7 μm to 3 μm. CO_2 absorbs in distinct narrow bands at 2.7 μm, 4.25 μm and 15 μm. Ozone absorbs infrared radiation at 9.5 μm. The relatively transparent bands ("windows") are 3-5μm and 8-13μm.

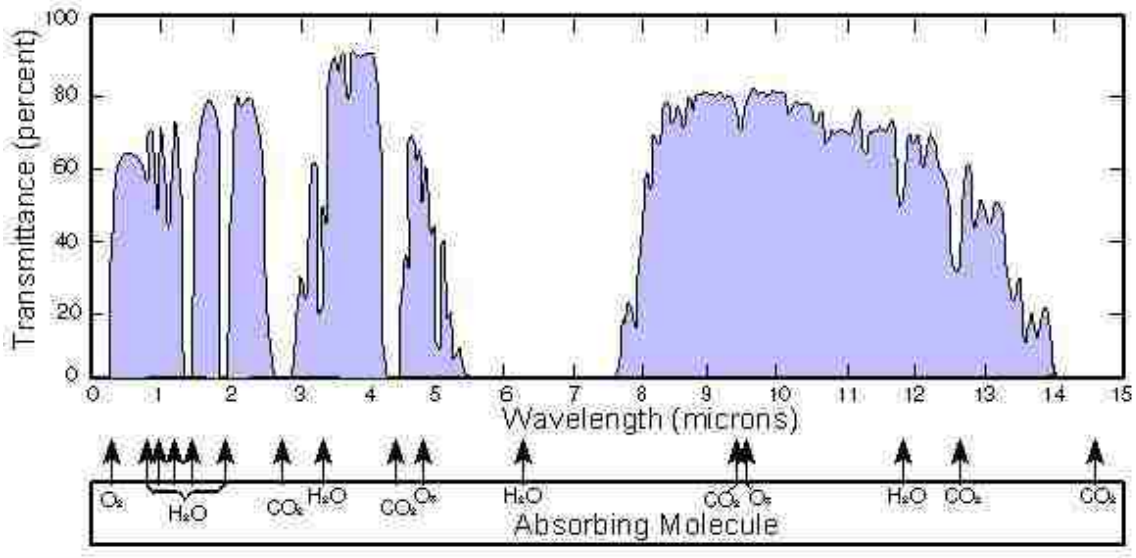

Figure 1.3 The Transmittance of the atmosphere[5]

Infrared radiation has been classified according to atmospheric windows into several bands. Near Infrared Radiation (NIR) spans from the end of the visible radiation, 0.7 μm to 1 μm; Short Wavelength Infrared Radiation (SWIR) covers the EM spectrum from 1 μm to 3 μm. The Mid Wavelength Infrared Radiation (MWIR) window is from 3 to 5 μm. The Long Wavelength Infrared Radiation (LWIR) is from 8 to 12 μm and the Very Long Wavelength Infrared Radiation (VLWIR) covers wavelengths 12 to 30 μm.

The LWIR window corresponds to the peak emission of a blackbody with a temperature of 300K.

1.3 Infrared detection

By constructing devices that can convert infrared radiation to a measurable signal, in most cases electrical, one can effectively detect the infrared radiation. Infrared detectors can be split into two different categories, according to the methods of conversion of EM radiation, thermal detectors and photon detectors.

1.3.1 Thermal Detectors

Thermal detectors are sensitive to external variation in temperature. This is a two step process; first the absorbed radiation on the detector changes the temperature of the detector, then the temperature change induces a measurable parameter change. Because of the nature of detection (response to the intensity of absorbed power), the response of thermal detectors is not dependent on the wavelength of incident light. The drawback of thermal detectors is that the incident radiation must change the temperature of the detector, so the response of thermal detectors is inherently slow. Three common

examples of thermal detectors are bolometers, thermocouples, and pyroelectric. Operation principles of these detectors are discussed further.

The operation of bolometers is based on the bolometric effect, which is change of the resistance of the responsive element with temperature change produced by the absorbed IR radiation. Bolometers are usually made of thin metal or semiconductor film with an absorbing film deposited on top of it and is suspended over a cavity in a substrate for thermal isolation. The electrical resistance of the film is monitored. When the temperature increases due to absorbed radiation, the film resistance changes, it increases if the film is metallic and decreases if the film is semiconductor.

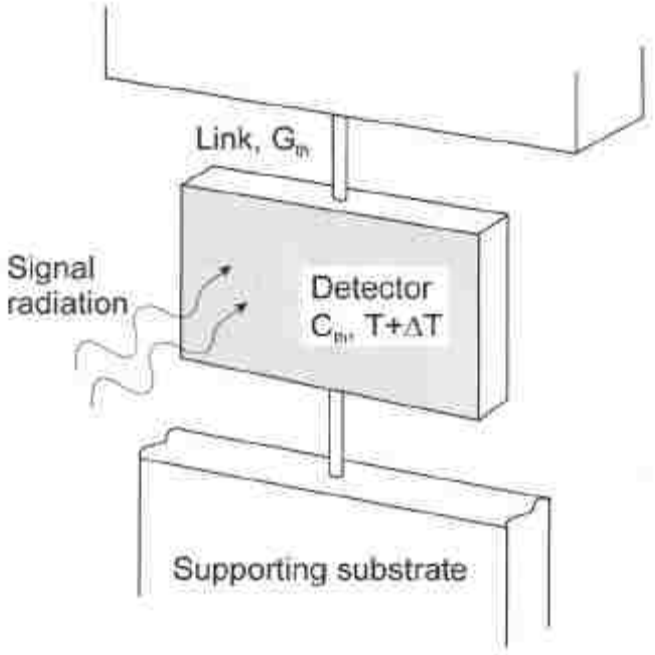

Figure 1.4 Schematic of a bolometer[6]

Thermocouples rely on the thermovoltaic effect which is that the separation between two different metals will change with change in the amount of incident radiation. This change in separation changes the voltage across the junction. Thermocouples connected

in series or parallel is called a thermopile and it used to increase the voltage output to a measurable level.

Pyroelectric detectors can operate at room temperature and are fairly inexpensive making them very common. Pyroelectric detectors operate when a change occurs in the temperature due to change in incident radiation which causes an electrical polarization of the material. This polarization change occurs on the surface of the element which creates a current. Pryoelectric devices have a broad spectral response in the infrared spectrum. The change of the polarization can vary rapidly in pryoelectric devices, but the response of the detector is still limited by the thermal properties of the material.

1.3.2 Photon detectors

Photon detectors operate by the direct interaction of radiation with the atomic lattice of the material. This interaction of light and matter produces electrical parameter changes that are detected by associated circuitry. Electrical parameters that can change in a photon detector are resistance, inductance, voltage and current. For photon detection the concept of creating an electron-hole pair from an absorbed photon must be understood. Quantum efficiency (QE), defined as the number of carriers measured at the output of the detector per number of incident photons per unit time, is used to understand this concept. External quantum efficiency is ideally unity for photodetectors, however in reality it is always less than that. The quantum efficiency relates the incident photons on the active area of the detector to the number of electrons generated, but excludes electrons generated by internal gain. If the energy of incident radiation is high enough, photons excite bound electrons to jump to the conduction band. The point where the photon no

longer has sufficient energy to excite an electron is called the cutoff wavelength, denoted (λ_c) and as shown in figure 1.5. From equation 1.2 one can calculate the cutoff wavelength.

$$\lambda_c = \frac{hc}{E_g} \tag{1.6}$$

Where E_g is the bandgap energy of the semiconductor material. The two main types of photon detectors are photoconductive (PC) and photovoltaic (PV) devices.

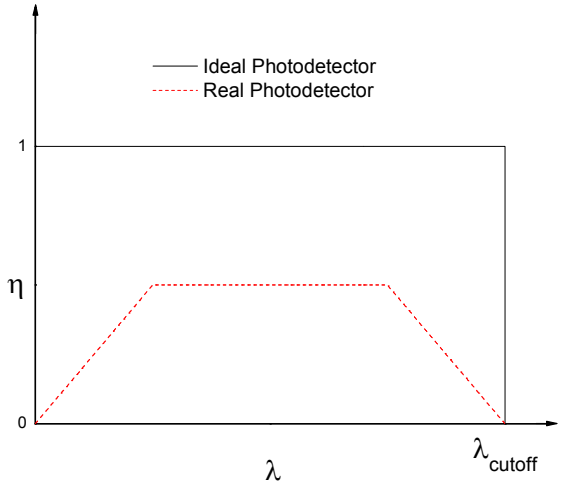

Figure 1.5 Quantum efficiency for ideal and real photon detectors

1.3.3 Photoconductive detectors

Photoconductors respond to radiation by changing the conductivity of the material. The resistance of the device is then inversely proportional to the amount of incident radiation. Intrinsic photoconductors absorb photons with energy above the bandgap energy of the semiconductor material as shown in Fig 1.6 (a). The bandgap of extrinsic materials depends on concentration of intentional impurities and they have absorption energies

much lower and λ_c much longer than intrinsic photoconductors as shown in Fig 1.6 (b & c). To prevent thermal ionization, extrinsic semiconductors need to be cooled. This means that intrinsic PCs can operate at higher temperature than extrinsic PCs, but that the λ_c of extrinsic PCs can be much longer.

Figure 1.6 Photogeneration in a) intrinsic, b) extrinsic n-type and c) extrinsic p-type photoconductors

To measure the change in conductivity, the PC must have an externally applied bias. The external biasing circuit creates an electric field to collect the photogenerated carriers by opposite contacts as shown in figure 1.7.

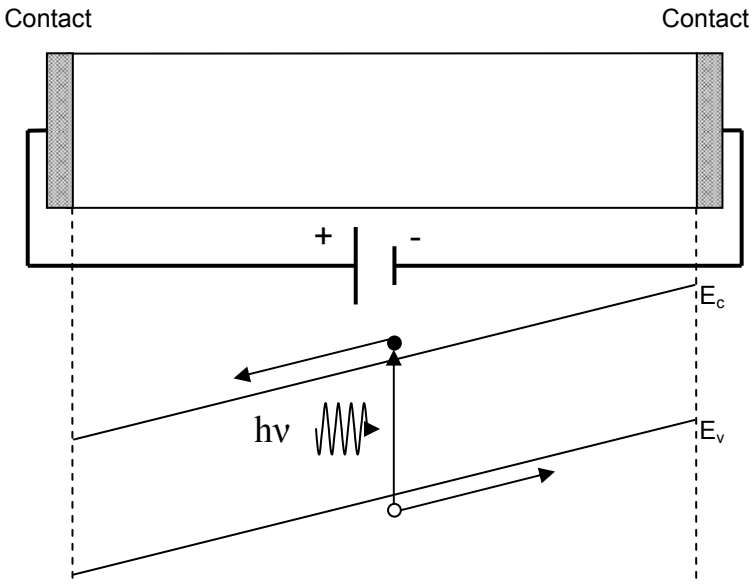

Figure 1.7 Schematic photoconductor with externally applied bias

1.3.4 Photovoltaic detectors

Optical detection in a photodiode occurs when a photon with energy greater than the bandgap excites an electron hole pair and the pair is separated by the built in electric field. Only carriers in the depletion region are separated by the built in field, so electron hole pairs outside a diffusion length of the depletion region recombine and do not contribute to the photocurrent. A PIN junction photodiode is depicted in Fig 1.8

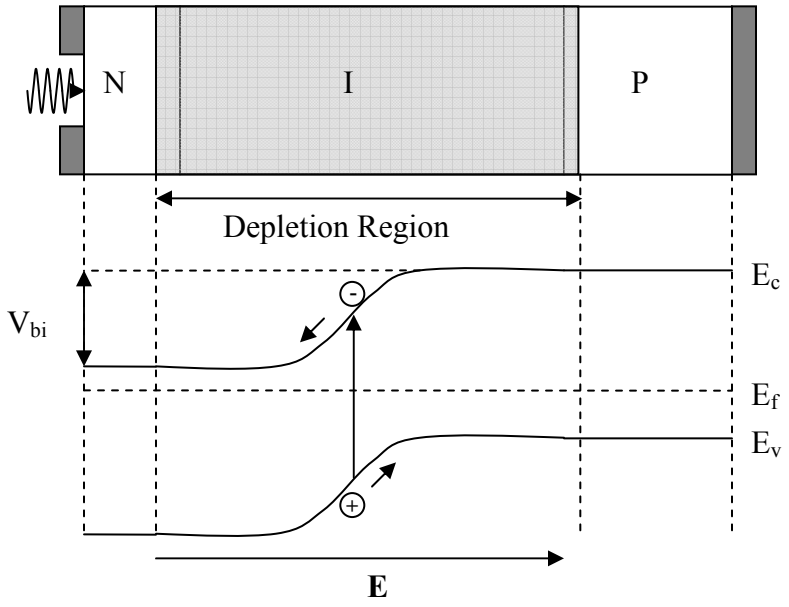

Figure 1.8 Schematic of p-n junction optical absorption

The diode current equation is given as

$$i = i_0\left(e^{\frac{qv}{bkT}} - 1\right) - i_g \tag{1.7}$$

where i_0 is the reverse saturation current, q is the charge on the electron, v is the voltage across the diode, b is the nonideality factor, k is Boltzmann's constant, T is the temperature and i_g is the photogenerated current, given by

$$i_g = \eta \phi_q q \tag{1.8}$$

where η is the quantum efficiency and φ_q is the photon flux measured in photons/sec. The addition of the photogenerated current shifts the IV curve of the photodiode so that there is an open circuit voltage (V_{oc}) and a short circuit current (I_{sc}) as shown in Fig. 1.9.

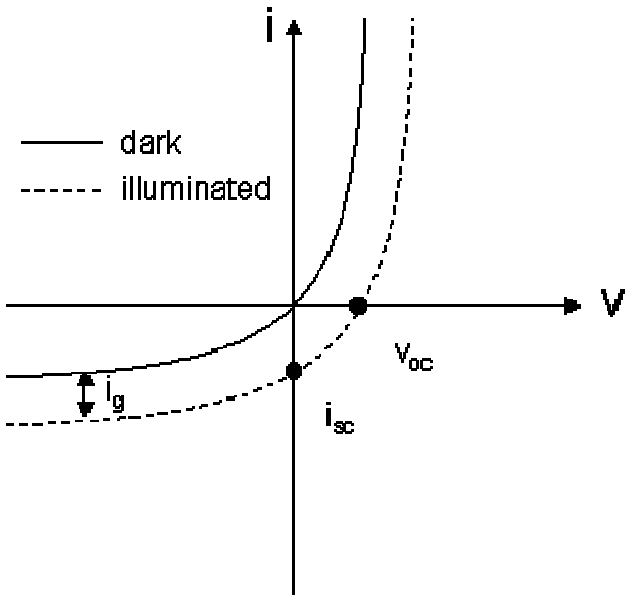

Figure 1.9 IV curve for ideal photodiode with and without incident radiation

The main advantage of a photodiode over a photoconductor is the dominant noise mechanism in a photodiode is shot noise which a factor of $\sqrt{2}$ smaller than the dominant noise mechanism in a photoconductor. Due to this, the SNR of photodiodes is usually higher than the SNR for photoconductors.

1.4 Figures of merit

There have been many different ways to describe a detector's performance through the course of their history. In an attempt to allow for comparison between different types of

detectors, figures of merit have been developed. The figures of merit allow for a comparison that is independent of detector technology. The general figures of merit include responsivity, the noise equivalent power, and specific detectivity. While the figures of merit characterize both thermal detectors and photon detectors, the units are mostly energy based because thermal detectors were developed first.

1.4.1 Responsivity

The responsivity relates the output signal of a detector to the radiant input. The radiant input is normally expressed in watts while the output signal is expressed in volts, called the voltage responsivity, or in amps, called the current responsivity. The spectral responsivity is defined as the responsivity in terms of wavelength while the blackbody responsivity gives the peak responsivity value. For photon detectors, the responsivity is related to the quantum efficiency. Using equation 1.8 as the expression for photogenerated current and φ_e as the radiant power (flux) input given in watts, the equation for the current responsivity is then

$$\Re_i = \frac{\eta \phi_q q}{\phi_e} \tag{1.9}$$

given in units of amps per watt. The radiant power is related to the photon flux by

$$\phi_e = \frac{hc}{\lambda}\phi_q \tag{1.10}$$

so the equation for current spectral responsivity becomes

$$\Re_i(\lambda) = \frac{\eta \phi_q q \lambda}{\phi_q hc} = \frac{\lambda}{hc} q \eta \tag{1.11}$$

Equation 1.11 gives the relation between quantum efficiency and current responsivity as a function of wavelength for photon detectors. The theoretical limit for current responsivity for different QE is given in Fig. 1.10.

The responsivity of a detector gives the expected signal for a given level of radiation. The responsivity does not provide information about the sensitivity of the detector, because no information is given about the noise in the detector. So the responsivity of a detector could be large but the performance of the detector could still be poor if the noise of the detector was also large.

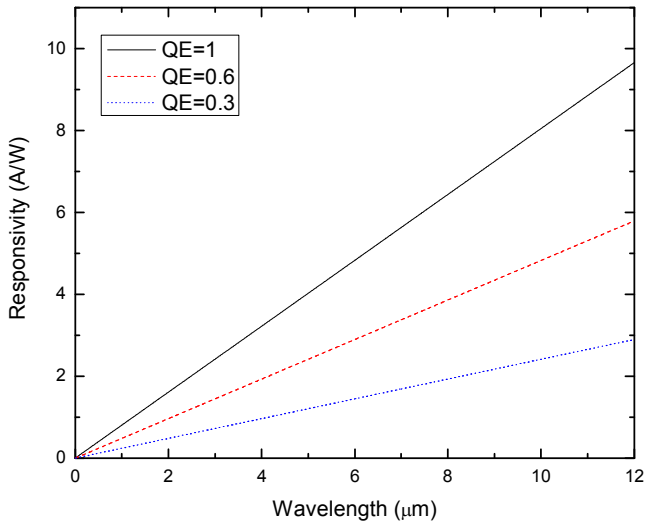

Figure 1.10 Peak current responsivity as a function of wavelength for ideal photon detector with different quantum efficiencies

1.4.2 Noise equivalent power (NEP)

The responsivity is the output signal divided by the radiant flux on the detector. The signal to noise ratio (SNR) of the detector is then

$$SNR = \frac{\Re_i \phi_e}{i_n} \tag{1.12}$$

where R_i is the current responsivity, φ_e is the radiant power, and i_n is the noise expressed as current. The noise equivalent power is, as the name suggests, the radiant input power that makes the noise equivalent to the signal or a SNR equal to 1. Setting the left hand side of equation 1.12 equal to 1 and solving for φ_e gives

$$NEP = \frac{i_n}{\Re_i} = \frac{\phi_e}{i_{sig} / i_n} \tag{1.13}$$

the units of which are watts. The NEP can also be found using the voltage noise and the voltage responsivity. The lower the value of NEP, the more sensitive the device. The NEP cannot be readily compared between different detectors because NEP depends on detector area and other measurement parameters. For direct comparison of any type or size detector under different operation conditions Jones[7] suggested a figure of merit called normalized detectivity.

1.4.3 Specific Detectivity (D*)

The specific detectivity (D*) is the SNR of a detector normalized to an area of 1 cm^2, with 1 W of radiant power incident on the detector with a 1 Hz noise bandwidth. D* is

$$D^* = \frac{\sqrt{A_d \Delta f}}{NEP} \tag{1.14}$$

where A_d is the area of the detector and Δf is the bandwidth of the measurement. D* can be related to the responsivity by

$$D^* = \frac{\Re_i \sqrt{A_d}}{i_n / \sqrt{\Delta f}} \tag{1.15}$$

The units of D* are cm $Hz^{1/2}$/watt which is called Jones after the creator of the figure of merit. D* allows for comparison between detectors regardless of size or measurement parameters.

1.5 Theoretical limit of detection

Using detector figures of merit defined in the previous section, expressions for the theoretical limit of detection can be derived. The best performance of a photon detector occurs when photon noise, noise caused by the absorption of a photon, is the dominant source of noise. When the photon noise from the signal is dominant it is called signal-dependant noise. This condition is rare for infrared detectors because the background is the usual dominant photon noise source. When the background is the dominant noise source the detector is said to be background limited infrared photodetector or BLIP. To find the BLIP limited D* for both types of photon detectors, the understanding of the dominant noise sources for PV and PC detectors is required. Shot noise, the noise from dc current flowing across a potential barrier is the dominant noise source in PV detectors. The equation for shot noise is

$$i_{shot} = \sqrt{2qi\Delta f} \tag{1.16}$$

if i is the result of incident photons then the detector is BLIP. One can show that the NEP for BLIP PV detector is

$$NEP = \sqrt{\frac{2E_q A_d \Delta f}{\eta}} \frac{hc}{\lambda} \tag{1.17}$$

where E_q is the incident photon flux. E_q depends on the detector geometry as shown in figure 1.11. E_q is then the photon flux exitance times $\sin^2 \theta$ known as the numerical aperture.

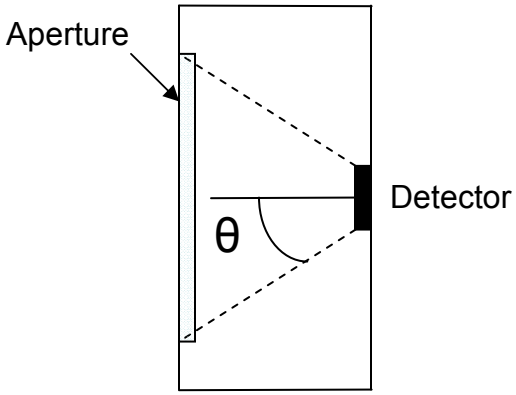

Figure 1.11 θ dependent aperture limit

From equations 1.14 and 1.17, D* is then

$$D^*_{BLIP} = \frac{\lambda}{hc} \sqrt{\frac{\eta}{2E_q}} \tag{1.18}$$

For PC detectors generation-recombination noise is the dominant noise source and is given by

$$i_{gr} = 2qG\sqrt{E_q A_d \eta \Delta f} \tag{1.19}$$

where G is the photoconductive gain. Following the same steps as for PV detectors

$$D^*_{BLIP} = \frac{\lambda}{2hc} \sqrt{\frac{\eta}{E_q}} \tag{1.20}$$

gives D* BLIP for PC. BLIP D* for PC is lower than BLIP D* for PV by the square root of two.

BLIP D* for an ideal thermal detector is given by

$$D^*_{BLIP} = \frac{1}{4 \cdot \sqrt{k\sigma T^5}} \tag{1.21}$$

where σ is Stefan-Boltzman constant and at 300K is equal to 1.8×10^{10} Jones.

From equations 1.18, 1.20 and 1.21 and using the limiting factor of the field of view (FOV) for the detector, the peak D* BLIP is shown as a function of wavelength in Fig. 1.12.

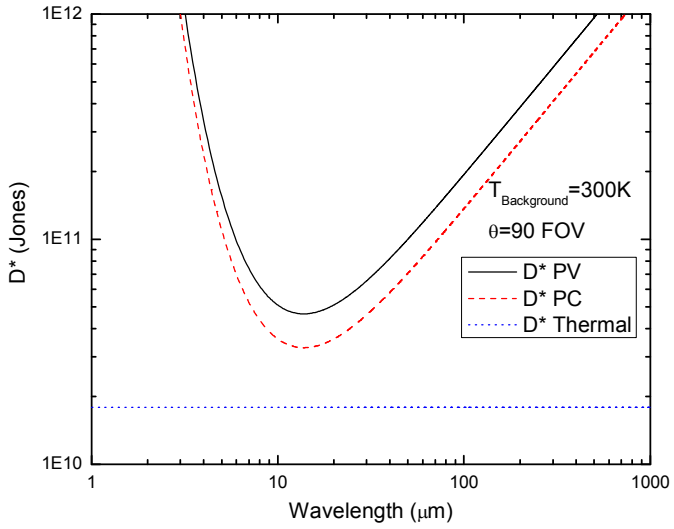

Figure 1.12 BLIP D* for ideal PV, PC and Thermal detector

While photon noise limited detector is desired, in low photon flux levels situations the best SNR is achieved when the detector is Johnson noise limited. Johnson noise limited (JOLI) D* for a PV detector is given by

$$D^*_{JOLI} = \frac{\lambda \eta q}{2hc} \sqrt{\frac{R_0 A_d}{kT_d}} \tag{1.22}$$

where T_d is the detector temperature and R_0A_d is the dynamic resistance at zero bias.

1.6 Focal Plane Arrays

A Focal Plane Array (FPA) is the main component used in advanced infrared imaging systems. An IR FPA is an array of single pixel devices used to capture an infrared signal. FPAs increase the efficiency of collection compared to a single pixel by decreasing acquisition time. Both thermal and photon detectors can be made into FPAs and each has their own advantages and disadvantages.

1.6.1 Thermal Detector FPAs

As mentioned in section 1.3.1 operation of thermal detectors depend on measurable parameter change produced by absorbed radiation. The main advantage of thermal detectors is that it can operate at ambient temperature. Another advantage is that the response is independent of wavelength, which is important for LWIR application. The main disadvantages for thermal detectors are the low detectivity (capped at $1.8x10^{10}$ Jones at 300K) and the slow response time which eliminates thermal detectors FPAs from being used for high performance applications. Applications for thermal detector FPAs include space based astronomy, thermal sensors, industrial monitoring including low cost handheld imagers for industrial applications.

Microbolometer arrays are made using silicon micromachining. Usually semiconducting vanadium oxide is used as the detecting material. This is placed atop a thin membrane typically silicon nitride and connected to the substrate by silicon nitride legs coated with conductive film. Microbolometers with 640x480 pixels are commercially available.[8]

1.6.2 Photon Detector FPAs

Materials for commercial photon detectors FPAs are HgCdTe, InSb, GaAs/AlGaAs and InAsSb. Each material system has its own inherent strengths and weaknesses.

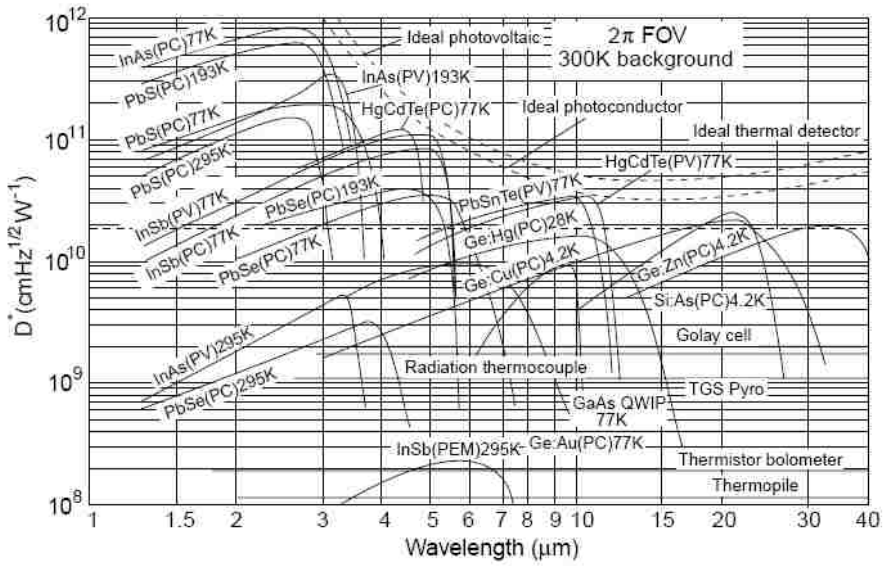

Figure 1.13 Comparison of commercially available infrared detectors at given operating temperature[9]

HgCdTe (MCT)

Infrared detectors HgCdTe (MCT) were first introduced in 1959 by Lawson et al.[10] $Hg_{1-x}Cd_xTe$ is made up of elements from column II and VI in the periodic table. It is a direct gap material whose bandgap can be varied from negative values (-0.1415 and -0.2608 eV at 300K and 77K) for HgTe to relatively large values for CdTe (1.4895 and 1.6088 eV at 300K and 77K) to give a cutoff wavelength a range from 1μm to 30μm.[11] The lattice constant difference between HgTe (6.414Å) and CdTe (6.4809 Å) is only 0.3% so the composition of the material can be chosen in any range between the two and still be relatively lattice matched. Also, the optical absorption coefficient is large

allowing for high quantum efficiency[11]. HgCdTe is the ideal material system for infrared detection but certain technological issues keep it from being completely dominant. The key disadvantages of HgCdTe are the uniformity, producibility, and cost. The growth of high quality HgCdTe is difficult due to large defect densities and large non-uniformity as the mole fraction of Hg is increased. The major noise mechanism are large tunneling currents due to low electron effective mass. Commercially available MCT FPAs have 640 x 480 pixels in LWIR with 27 x 27 μm pixels and 640 x 512 pixels with a pixel size of 24 x 24 μm in MWIR[9]. 1280 x 1024 pixel FPAs grown on germanium substrates with square 15 x 15 μm pixels have been reported[12]. HgCdTe is the material system against which other variable bandgap materials are judged.

InSb

Indium Antimonide (InSb) detectors are widely used for MWIR applications because of the bulk properties of the material. The bandgap of InSb is 0.180 eV at room temperature and 0.228 eV at 80K corresponding to λ_{cutoff} of ~7μm and 5.5μm respectively. Thermally generated carriers are the dominant noise source at high temperature requiring InSb detectors to be cryogenically cooled. Large uniform substrates are available allowing for fabrication of large area FPAs (1024 x 1024). InSb detectors are used in forward looking infrared heat seeking missiles and thermal imaging. The drawbacks of the material system include the requirement of cooling, the material specific cutoff wavelength limit and the tendency of the FPA characteristics to drift between uses.

Quantum Well Infrared Photodetector - QWIP

Quantum Well Infrared Photodetectors are a relatively new type of IR photodetector that employs bandgap engineering and quantum size effects. Bandgap engineering is made

possible by the precise control of constituent material layer thickness and doping concentration by using molecular beam epitaxy (MBE) and metal-organic chemical-vapor deposition (MOCVD). Using bandgap engineering LWIR photodetectors can be made using III-V materials whereas the bulk III-V material with the longest cutoff wavelength is InSb with a λ_{cutoff} of 5.5μm. The most researched QWIP is made using GaAs/AlGaAs. GaAs/AlGaAs QWIPs are grown on GaAs substrates due to small lattice mismatch between AlGaAs and GaAs thus taking advantage of mature GaAs growth technology. GaAs layers sandwiched between AlGaAs layers form quantum wells (QW). The energy levels of the QW are determined by the height and width of the well. Electrons in the ground state are photoexcited to the higher energy state. An applied bias lowers the potential barrier allowing the electron to tunnel out of the well.

MWIR FPAs with 1028 x 1028 pixels with NETD of 17mK at 95K have been reported[13]. Because of selection rules in quantum wells normal incidence light cannot be absorbed. For this reason diffraction gratings must be used to couple light into the QWIP for detection. The quantum efficiency for QWIPs (~20%) detectors is then much lower than for HgCdTe and InSb detectors. Thermally generated and quantum mechanical tunneling of carriers increase the dark current in QWIPs thus lowering the SNR, and limiting the peak operating temperature.

1.7 InAs/Ga(In)Sb Type II Strain Layer Superlattice

Smith and Mailhiot introduced the application of InAs/GaInSb strain layer superlattice as a possible alternative to HgCdTe in infrared imaging in 1987[14] using the semiconductor superlattice introduced by Esaki et al[15]. The superlattice structure is made up of

alternating layers of thin semiconductor material. The electronic structure of the superlattice depends on the layer thickness and periodicity of the constituent superlattice material[16]. Technological advancements in epitaxial growth of semiconductors allow precise control of layer thickness. The valence band of the higher bandgap energy GaSb is above the conduction band of the lower bandgap energy InAs. This is what is known as a type-II broken band offset and because of this band lineup the bandgap of the superlattice can be smaller than the bandgap of either of the constituent materials. The schematic band structure is shown in Figure 1.14.

The precise control of layer thickness and material composition enables engineering of the electronic band structure. There have been many different approaches to theoretically model superlattice semiconductor band structure. In the 1980s Smith and Mailhiot[17,18] analyzed semiconductor superlattice band structure using **k·p** theory. Dente and Tilton used the empirical psuedopotential method (EPM)[19] for superlattice materials including GaAs/AlGaAs, InAs/GaSb and AlSb/InAs/InGaSb/InAs and updated and applied it to InAs/GaSb superlattices[20] later. Wei and Razeghi applied an empirical tight-binding method with consideration of interface engineering to model type-II InAs/GaSb superlattices.[21]

Using InAs/Ga(In)Sb material system the cutoff wavelength can be tailored over a wide range from 3μm to 30μm. Different combinations of superlattice periodicity or constituent material composition can be used to achieve the same superlattice bandgap. InAs/Ga(In)Sb is seen as a possible material system for third generation FPAs.[22] InAs/Ga(In)Sb SLSs have high responsivity because of their strong absorption of normal incidence light and because of this, higher QE than QWIPs. Also, InAs/Ga(In)Sb operate

at elevated temperatures and use established III-V technology. The advantages that InAs/Ga(In)Sb may hold over HgCdTe include lower tunneling current since the band-edge effective masses in InAs/Ga(In)Sb are not directly dependent on the band gap energy and are larger than HgCdTe at the same bandgap. Another advantage is commercially available GaSb substrates with good electro-optical homogeneity without large cluster defects. Also, in this material system the probability of finding electrons and holes are localized to InAs and Ga(In)Sb layers respectively. This suppresses Auger recombination, which leads to longer carrier lifetime and higher QE [23]. Further advancements are required in InAs/Ga(In)Sb SLSs especially for material growth, processing, substrate preparation and device passivation.[24]

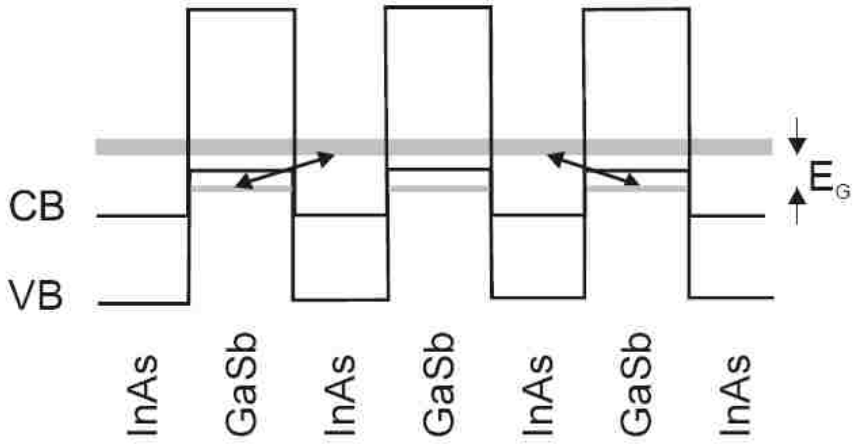

Figure 1.14 Superlattice schematic band structure and absorption process[25]

Device passivation is especially difficult as the device cutoff wavelength increases. The spatial separation of electrons and holes decrease the optical absorption, but this can be overcome by the introduction of InSb to the GaSb layers which increases the cutoff wavelength without increasing the layer thickness.

1.7.1 Type II strain layer superlattice devices

Table 1.1 provides an overview of different superlattice single pixel detector performance results.

Superlattice Type	Device Type	λ_c	η	D*	Ref.
9.5 ML InAs / 12 ML GaSb	n-on-p	5.4 µm @ 77K	30%	10^{13}	[26]
8 ML InAs / 11 ML GaSb	n-on-p	5 µm @ 300K	25%	10^{9}	[27]
9 ML InAs / 4 ML GaSb	n-on-p	7 µm @ 77K	12-32%	10^{12}	[28]
14 ML InAs / 7 ML GaSb	n-on-p	11 µm	36%		[29]
13 ML InAs / 7 ML GaSb	n-on-p	12 µm	54%	$2x10^{11}$	[30]
W-Structure 14 ML InAs / 9 ML GaSb / 14 ML InAs / 7 ML Al0.4Ga0.49In0.11Sb	p-on-n	10.5 µm @ 78K	20-34%		[31]
M-Structure 13 ML InAs / 7 ML GaSb 18 ML InAs / 3 ML GaSb / 5 ML AlSb / 3 ML GaSb	n-on-p	10.5 µm @ 77K 6 µm	27%		[32]
12 ML InAs / 7 ML GaSb	p-on-n	11 µm	20-35%		[33]
8 ML InAs / 8 ML GaSb	nBn	5.2 µm @ 300K	18%	10^{9}	[34]
9 ML InAs / 10 ML GaSb	n-on-p	5.4 µm @ 73 K	30%		[25]
8.6 ML InAs / 5 ML $Ga_{0.75}In_{0.25}Sb$	n-on-p	~10 µm @ 77K			[25]
Dual Band		11.4 µm and 17 µm			[35]
Dual Band	nBn	4.5 µm and ~8µm			[36]

Table 1.1 Superlattice device designs and parameters

1.8 nBn detector

The nBn detector introduced by S. Maimon and G. W. Wicks is a new class of infrared photodetectors designed to improve detector performance by reducing the dark current and increasing the operating temperature.[37] The nBn heterostructure design has demonstrated a 100 K increase in background-limited infrared photodetection (BLIP) for an InAs-based device, by decreasing Shockley-Read-Hall (SRH) generation currents and by suppressing surface currents using specific processing.

The reported nBn detector consists of an n-type narrow bandgap absorbing layer (InAs), a wide bandgap barrier layer ($AlAs_xSb_{1-x}$) and an n-type narrow bandgap (InAs) top contact layer.[37] The wide bandgap layer was chosen so that there was zero valence band offset where x~0.15. The barrier effectively blocks the flow of the majority carriers between the electrodes but allows the photogenerated carriers to be collected. The schematic band diagram of the nBn detector is given in Fig. 1.15.

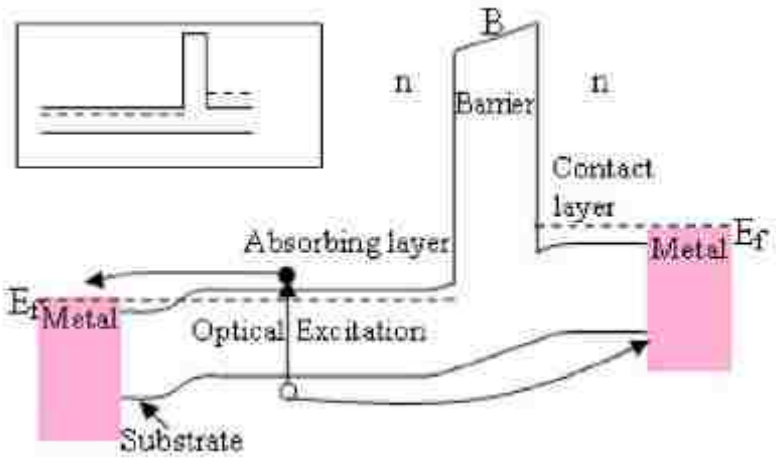

Figure 1.15 Band diagram of InAs-based nBn structure, biased under operating and flatband (inset) conditions[34]

There are three major dark current mechanisms in photodiodes based on narrow bandgap semiconductors. The first is SRH generation current in the depletion region of a photodiode. The second is radiative or nonradiative diffusion current in the extrinsic area. And third is the surface current that is controlled by passivation of the device. The nBn detector significantly reduces two of the three dark current sources. SRH generation is very efficient in the depletion region of a pn junction because of the activation of trap states and is considered the main source of dark current in MWIR photodiodes below 200K.[38] The nBn detector depends on the heterostructure barrier to block the flow of majority carriers through the device instead of the built-in barrier of the pn junction. The nBn is designed to operate in either flatband or with very little depletion. The nBn detector eliminates the pn junction so there is no depletion region and the device relies primarily on diffusion of the carriers. The surface current in the nBn detector is eliminated by the way the device is defined and processed. The nBn detector is etched only to the barrier not to the bottom contact layer like in a conventional mesa etch. This suppresses the surface current by eliminating the etched sidewalls. Also, the barrier then acts as a passivation layer for the device and no further passivation is needed. The final source of dark current in a pn junction is thermal generation in the neutral region of the device. This current source is still present in the nBn detector and will not be suppressed. This is a major advantage for the nBn detector over other detectors that are limited by SRH when operating in BLIP conditions. The expressions for the current density for SRH generation (J_{SRH}) and diffusion (J_{diff}) are

$$J_{SRH} \approx q \frac{n_i}{\tau_{SRH}} W_{dep} \tag{1.23}$$

where n_i is the intrinsic carrier concentration, W_{dep} is the depletion width, τ_{SRH} is the SRH lifetime of the carriers which depends on the quality of the material, and

$$J_{diff} \approx qp_n \frac{1}{\tau_{diff}} L = q \frac{n_i^2}{N_d} \frac{1}{\tau_{diff}} L \tag{1.24}$$

where τ_{diff} is the lifetime, L is the smaller of the width of the neutral region of the device or the diffusion length of the minority carriers, p_n is the hole concentration in the n-type semiconductor and is equal to n_i^2/N_d. The activation energy of the SRH current is then proportional to $E_g/2$ because of the dependence of the current on n_i ($n_i \sim \exp(-E_g/2kT)$), while the diffusion current is dependent on n_i^2 so that the activation energy is proportional to the bandgap E_g ($n_i^2 \sim \exp(-E_g/kT)$). The two lifetimes are usually the same order of magnitude and W_{dep} and L are comparable so as long as $n_i > n_i^2/N_d$ the pn junction will be SRH limited. The nBn eliminates the SRH current and so its activation energy is E_g whereas a pn junction has an activation of $E_g/2$. The factor of two difference means that the nBn can operate with similar performance at about twice the temperature.

The nBn detector is a class of detector like the pn junction so it can be extended to other material systems. Recently, the nBn design has been extended to InAs/GaSb superlattice material utilizing an AlGaSb barrier layer, and an MWIR detector (cutoff wavelength (λ_{cutoff}) at 5.2 μm) has been reported.[32] Utilizing band gap tunability of InAs/GaSb SLS material, the operation wavelength of the nBn detector based on such SLS can be extended to the LWIR and VLWIR regime.

1.9 Conclusion

In this chapter the fundamentals of infrared detection were presented. IR detector figures of merit were discussed in detail. Competitive third generation FPAs material systems

were covered with their disparate strengths and weaknesses, providing motivation for continued research using other material systems. Superlattice detectors and their merits as a possible alternative for third generation FPAs were outlined. This chapter provides the foundation upon which all of the following chapters rest. The remaining chapters cover the specifics of SLS IR detectors measurement and the research toward increasing the operating temperature by using nBn superlattice detectors.

2 Materials and Methods

This chapter covers the experimental methods required for testing of infrared photodetectors. The first section covers Molecular Beam Epitaxy (MBE) technique specifically for growth of InAs/GaSb SL. MBE growth of superlattice material is the first step in the realization of IR photodetectors. After growth the next step is device processing. A basic outline of processing is given while a detailed example is given is Appendix A. The focus of this section will be the processing of single pixel devices. Measurement techniques will be given for classifying the performance of single pixel devices to find the spectral response and responsivity other and figures of merit introduced in the previous chapter (λ_{cutoff}, Responsivity, QE, D*).

2.1 Molecular Beam Epitaxy (MBE)

The Molecular Beam Epitaxy (MBE) technique was invented by Alfred Cho of Bell Telephone Laboratories in the late 1960's. MBE is an Ultra High Vacuum (UHV) system for growing single crystal materials on prepared substrates using elemental sources. The mean free path of particles in UHV is much greater than the distance from the source to the substrate so that there is no particle interaction with anything before reaching the substrate. Due to the low growth rate (less than an atomic monolayer per second) and the ability to shutter the beam of particles within a fraction of a second, MBE improved the control of semiconductor growth so that epitaxial layers could be deposited with good control of thickness, composition and doping.

The material presented in this work is grown in a VG-80 MBE solid source two sided reactor. This MBE system consists of a two identical growth chambers, a preparation chamber and a load lock.

The load lock is used to bring in epi-ready substrates from the outside for growth or to remove a grown sample for processing while maintaining the vacuum integrity of the chambers. The load lock is a canister with seals on the topside towards the atmosphere and the bottom facing the prep chamber. The canister contains slots for the substrate holders to be placed. To introduce a sample the load lock must be dumped to atmosphere, the sample inserted into the cassette and then pumped down to vacuum ($1x10^{-8}$ Torr) using a combination of a mechanical roughing pump and a turbomolecular pump.

The preparation chamber is used for substrate transfer, substrate storage and substrate heating for initial outgassing. The preparation chamber is equipped with a trolley system used to transfer samples under vacuum conditions to the growth chambers. The preparation chamber is equipped with an ion pump to maintain vacuum conditions and an ion gauge to monitor the vacuum level.

Each of the growth chambers contain all the necessary components needed for crystal growth. To achieve UHV level (pressure $\sim 10^{-10}$ Torr) the growth chamber is equipped with an ion pump, a He closed loop cryopump and a Titanium sublimation pump. The stainless steel shroud around the growth chamber is filled with Liquid Nitrogen (LN_2). This Cryo-shroud captures residual gases and is considered the most important pump during growth. The sources of material for growth are conventional effusion and dissociation effusion (cracker) cells each equipped with an individual shutter. The manipulator assembly contains the substrate holder that heats and rotates the substrate,

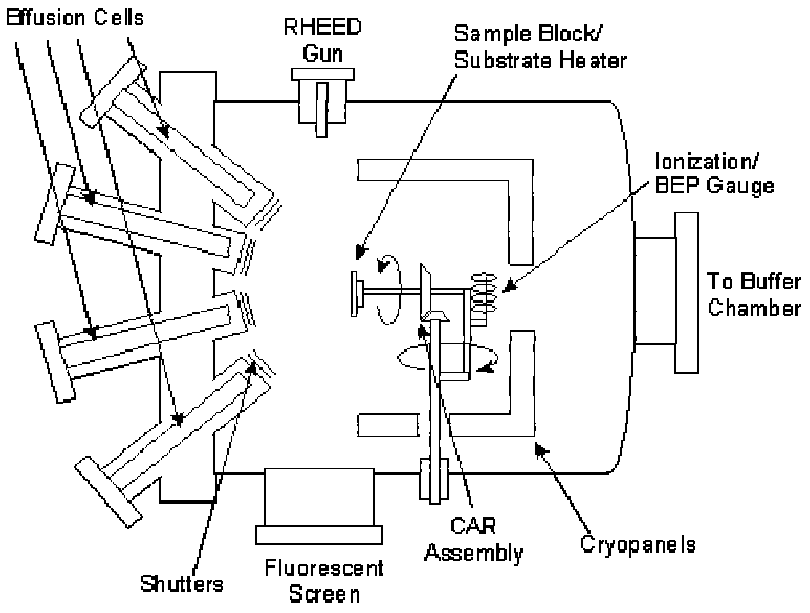

Figure 2.1 Schematic of a Molecular Beam Epitaxy growth chamber

thermocouple to monitor substrate temperature, and an ion gauge to monitor the beam equivalent pressure. The growth chamber also includes an optical pyrometer for accurate substrate temperature readings, a mass spectrometer to monitor residual gas levels (CO_2, H_2O, N_2 and CO), a Reflection High Energy Electron Diffraction (RHEED) gun and fluorescent screen for *in situ* monitoring of the growth process. Schematic picture of growth chamber is shown in Fig. 2.1.

Effusion cells are used to evaporate materials during growth. There are two different types of effusion cells used, a conventional effusion cell and a dissociation (cracker) effusion cell. The conventional effusion cell consists of a pyrolitic boron nitride crucible that is surrounded by a heating element. Temperature of the cell is controlled by a thermocouple. The crucibles are filled with group III elements (Al, Ga and In) as well as dopant materials (Si, Be, GaTe). The flux rate is controlled by the temperature of the cell. Dual filament cells offer separate temperature control of the tip and the base of the cell

and are used to improve growth uniformity by reducing spitting. Dissociation effusion (cracker) cells are used to reduce the group V (Arsenic and Antimony) sources tetramer molecules (As_4 and Sb_4) to dimeric molecules (As_2 and Sb_2). Valved crackers allow control of the Beam Equivalent Pressure without changing the temperature, but by opening and closing a valve. Shutters in front of the sources are controlled by a computer program are used to block the sources when they are not in use.

During the growth of InAs/GaSb SL the average lattice constant of the SL is different from than the GaSb substrate. The slight lattice mismatch is reduced through the control of heterojunction interfaces during SL growth. MBE technique allows careful control of interfaces to produce the desired interface composition. The hetero-interface can be approximated either "InSb-like" or "GaAs-like" interfaces (Ga/Sb/In/As or Sb/Ga/As/In respectively). InSb causes compressive strain and GaAs caused tensile strain. Mixed interfaces formed during InAs/GaSb SL growth are illustrated in Fig 2.2.

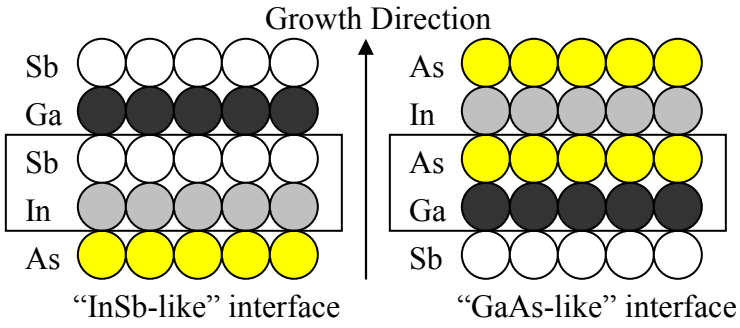

Figure 2.2 Schematic of possible interface

The alternating nature of the type of strain introduced either compressive strain for InSb interface or tensile strain for GaAs interface alters the structural, optical and electrical properties of the SLS.[39] To verify the high quality detector material growth, lattice

mismatch between the SLS and the GaSb substrate has to be equal to zero. Proper choice of shutter sequence during SLS growth (as illustrated in Fig. 2.3) enables compensation of lattice mismatch between SL and substrate.

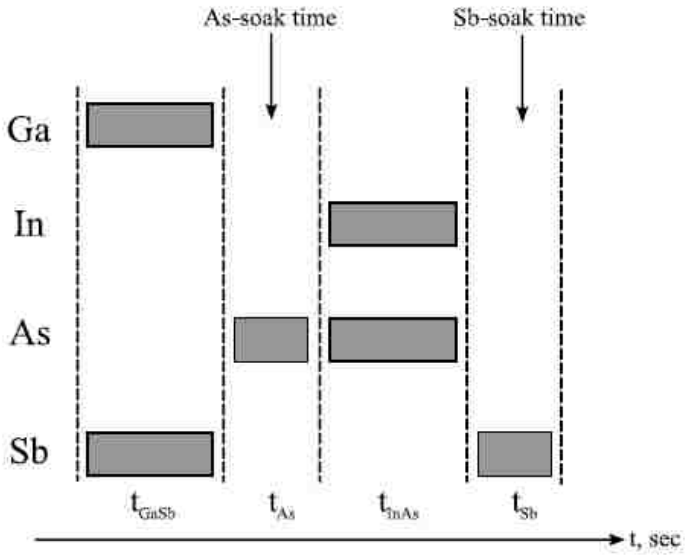

Figure 2.3 Shutter sequence for mixed interface growth

A typical cross-sectional Tunneling Electron Microscope (TEM) image of InAs/GaSb SL grown on MBE is given in Fig. 2.4.

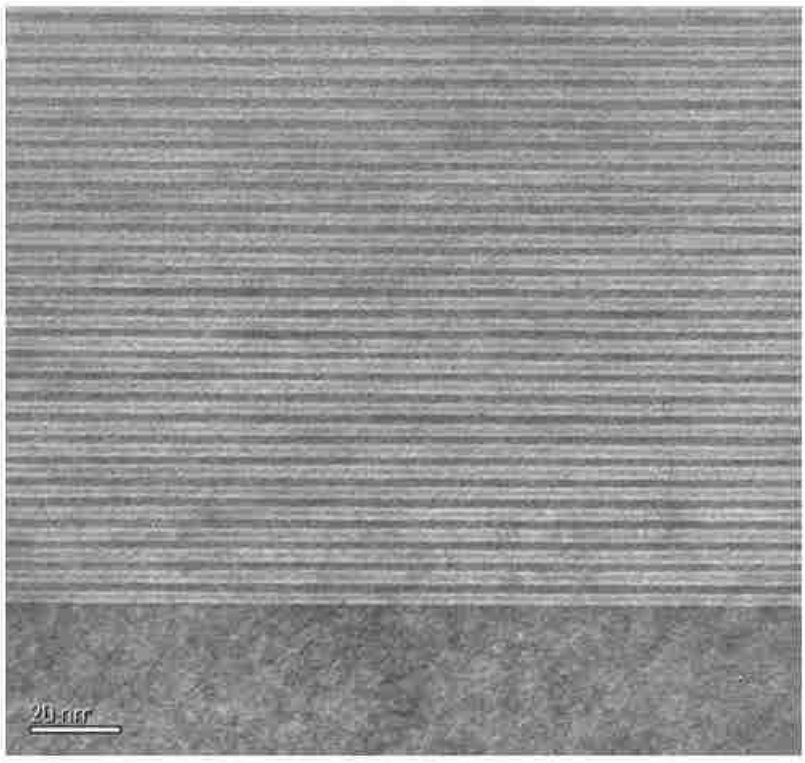

Figure 2.4 Cross-sectional TEM image of type-II superlattice undertaken at JPL[40]

2.2 Superlattice device processing

After growth the detector sample is processed into a device. Single pixel devices are used to approximate the performance of a FPA processed out of the same material. The steps required for conventional single pixel processing are described below. Basic processing sequence can be divided into three steps, top contact metallization, mesa isolation etch and bottom contact metallization. See Appendix A for complete processing details.

Optical photolithography is used for the metal pattern definition. The typical steps in a photolithographic process are the following: wafer cleaning, dehydration bake, adhesion

promoter application, photoresist application, softbake, exposure and develop cycle. The wafer is cleaned using acetone, isopropanol (IPA) and de-ionized (DI) water. Then dehydration bake is performed. After pretreatment, the sample is primed with hexamethyldisilazane (HMDS) on a spinner to promote adhesion and then baked. The next step negative photoresist is spun on and then baked. Using Mask 1 in Fig. 2.5(a) the sample is then exposed on the mask aligner, then baked, then flood exposed again without the mask for resist reversal. After the final exposure, the sample was developed leaving the photoresist in the desired places for metal deposition. After photolithography, the metal contact is deposited. We used Ti (500 Å)/Pt (500 Å)/Au (3000 Å) to achieve ohmic contact.

The next step is the mesa isolation etch. The photolithographic steps for the mesa isolation etch are similar to the steps used for top contact metallization. First the sample is pretreated and primed. Then positive resist was spun on and baked. Using Mask 2 in Fig. 2.5(b) the sample was exposed on the mask aligner. Finally the sample was placed in developer diluted in four parts water and developed.

The mesa isolation etch used wet chemical etching and etched to the bottom contact layer. The chemical composition is

$$H_3PO_4 : H_2O_2 : H_2O = 1 : 2 : 20 \qquad (2.1)$$

with an etch rate of 0.08 μm/min. The surface quality after etch shows no considerable degradation. After the mesa isolation etch, photoresist is applied as it was for the top contact metallization except Mask 3 in Fig. 2.5(c) is used. The bottom contact metal is Ti (500 Å)/Pt (500 Å)/Au (3000 Å) is then applied. Finally the sample is soaked in acetone for lift-off.

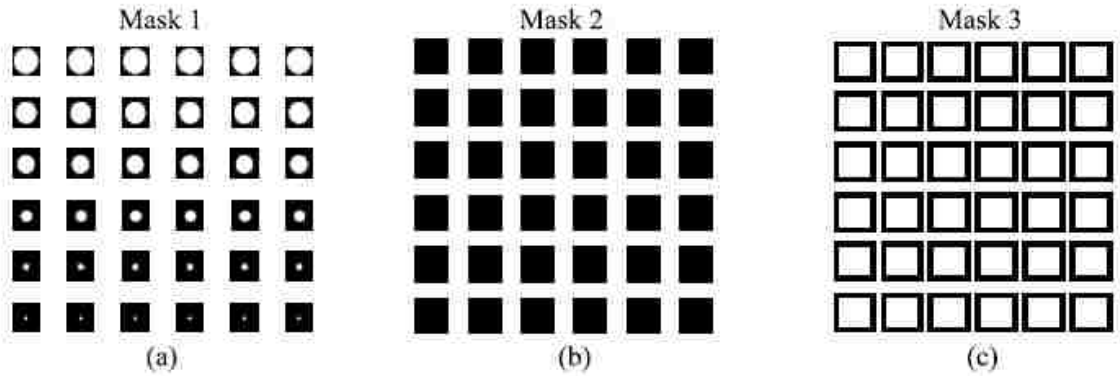

Figure 2.5 Mask designs used in fabrication of single pixel detectors

The final mesa size of a single-pixel device is 410 x 410 μm. The aperture diameters vary in size and are 300, 200, 150, 100, 50 and 25 μm. The schematic of the fully processed single-pixel photodiode with contact metallization is shown in Fig. 2.6.

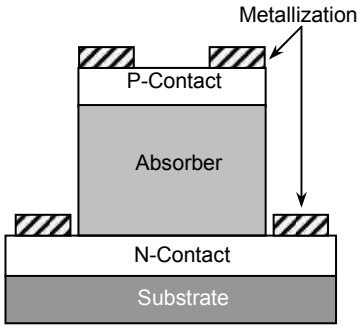

Figure 2.6 Conventionally defined PIN photodiode

2.3 Characteristics of Detector Performance

The processed devices were cleaved or individually diced and wire-bonded to a leadless chip carrier (LCC). To evaluate the electrical and optical performance of photodetectors the device to be tested was placed in a close-cycle Helium cryostat. Temperature

dependent IV characteristics of the devices were measured using a HP4145 Semiconductor Parameter Analyzer. Measurements were performed in 10K-300K temperature range. Dynamic impedance-area product (R_dA) is given by

$$R_d A = A\left(\frac{dI}{dV}\right)^{-1} \tag{2.2}$$

where A is the mesa area of the detector and the derivate is calculated from the measured IV data. For BLIP conditions, the background of the measurement determines the photocurrent generated. The orientation of the cold shield inside the cryostat can be either open to the room temperature background (room temperature background IV) or can be rotated so that the detector sees a cold radiation shield (dark current IV). As long as the detector is not background limited, there is little difference between the RT IV and the dark current.

The spectral response of the sample is measured using a Fourier Transform Infrared (FTIR) spectrometer. The FTIR contains a glow bar source, a Michelson interferometer with a movable mirror, an internally mounted Deuterated triglycine sulfate (DTGS) detector and mirrors to control the direction of the IR beam. The IR radiation from the glow bar source is put through the Michelson interferometer with the movable mirror to produce an interference pattern (which is the Fourier transform) of the spectrum of the IR source. For the spectral response measurement, the IR beam is directed outside of the FTIR off of a parabolic mirror and onto the detector mounted in the close-cycle He cryostat. The signal from the detector is then amplified by a preamplifer and fedback to the FTIR. Using computer software the inverse fourier transform is performed and the spectral response curves are then graphed and saved.

The DTGS detector measures the background source power spectrum and has a spectral response that is essentially flat. However, the intrinsic slow response of the detector combined with the high frequency modulation at the fringes of the interferometer signal cause the output of the detector to decrease as the modulation of light increases even above just a few hundred Hertz.[41] This creates a wavelength dependent gain in the DTGS detector. To create a gain curve, the output signal of the DGTS detector was measured with a 980 nm diode laser directly illuminating the DTGS detector. The laser was modulated using a sine wave source from 400 Hz to 10 kHz. Using the equation

$$f = nv \tag{2.3}$$

where f is the frequency (Hz), n is the wavenumber (cm^{-1}) and v is the velocity (cm/s) of the mirror, the DTGS detector correction curves were constructed as a function of wavenumber as shown is Fig 2.7. The DTGS correction instruction manual is given in Appendix B.

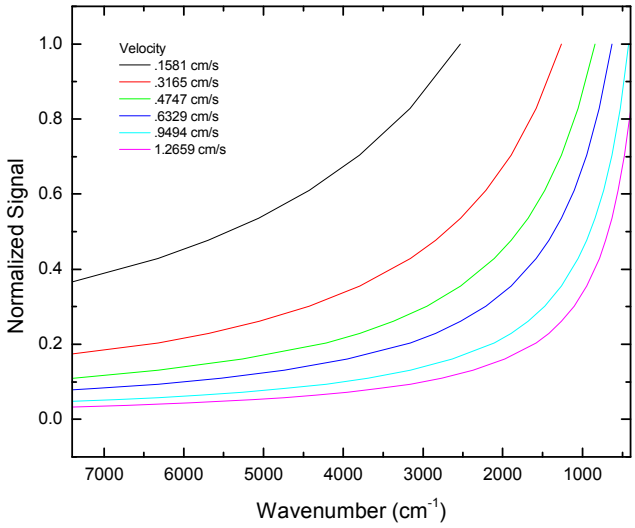

Figure 2.7 DTGS detector correction curves for different FTIR mirror velocities

The background spectrum (Fig. 2.8) is then divided by the gain curve (Fig. 2.9) to give a corrected background (Fig. 2.10). The spectral response of the SL detector (Fig. 2.11) is then divided by the corrected background and normalized to give the relative spectral response of the SL detector (NR(λ)) (Fig. 2.12). This spectral response is then used to in combination with the other radiometric measurements like the black body responsivity to determine the figures of merit for the detector.

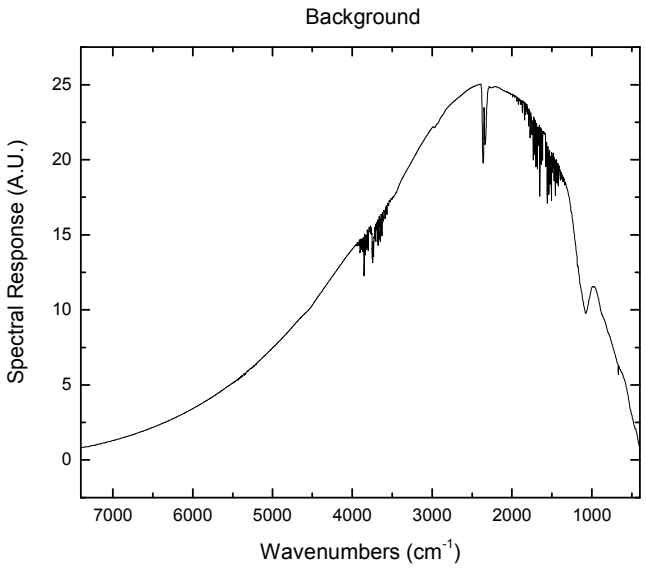

Figure 2.8 Background spectrum measured by DTGS detector

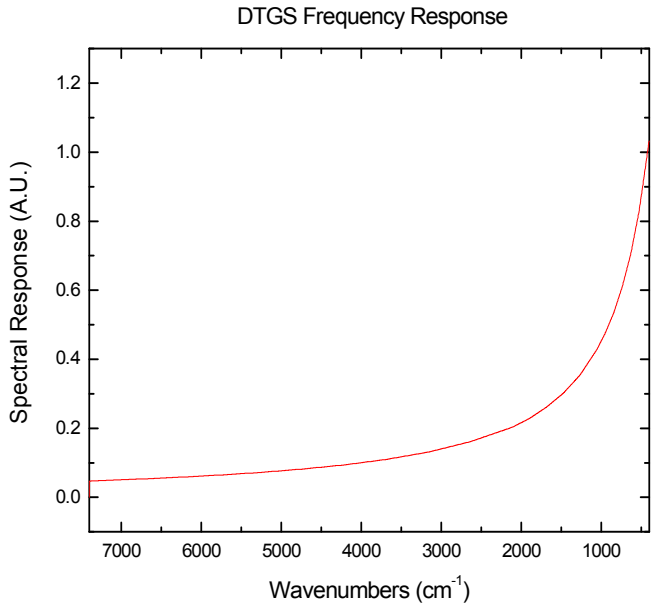

Figure 2.9 Correction Curve as a function of wavenumber

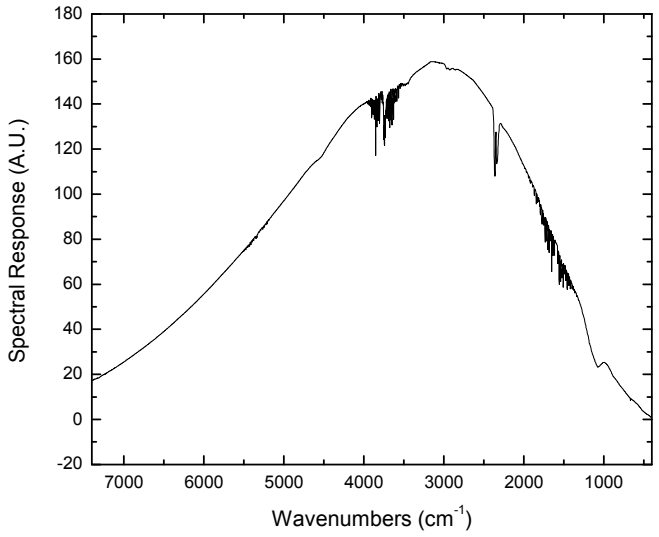

Figure 2.10 Background spectrum after division by correction curve

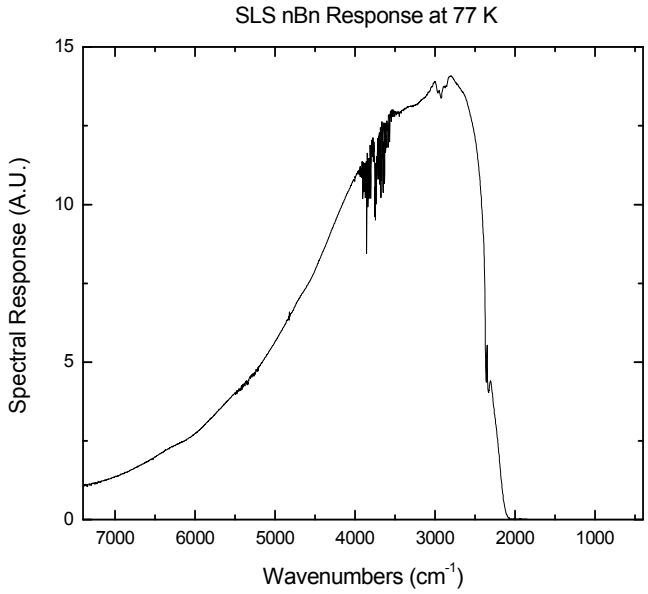

Figure 2.11 Superlattice detector sample spectral response without correction

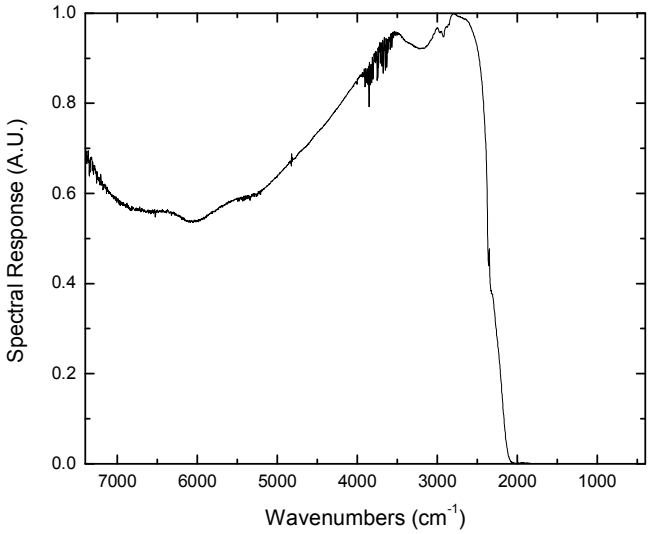

Figure 2.12 Final normalized and corrected SL detector spectral response (NR(λ))

2.3.1 Responsivity and D*

Responsivity for detectors is defined as the amount of current produced by the incident radiant power flux as given in Eq. 2.3.

$$\Re = \frac{signal}{\phi_e} \tag{2.3}$$

The signal of the detector is a measured quantity but the incident photon flux is estimated using radiometry. One way to find the spectral responsivity of the SL detector is to take the normalized spectral response (NR(λ)) as measured in Section 2.3 and multiply it by the peak responsivity (R_{max}).

$$\Re(\lambda) = R_{\max} NR(\lambda) \tag{2.4}$$

The experimental setup for responsivity measurements is shown in Fig. 2.13. This is used to measure the detector signal. The infrared radiation from the calibrated blackbody source at a temperature set by the temperature controller is radiated through a chopper onto the SL sample that is mounted in a pour filled dewar and cooled with LN_2. The chopper is used to periodically modulate our source so that the signal of the detector can be treated experimentally as the sum of a number of separate sinusoidal waves. The result is what is known as a Fourier series. The first term of the series is the fundamental frequency and is the same as the frequency of the chopper[3]. The electrical signal produced by the detector is then amplified by the current amplifier. The signal of the fundamental frequency is then measured using a FFT network analyzer. The radiant power (φ_e) in watts from the blackbody on the detector can be estimated by

$$\phi_e = \int_0^{\lambda_{cut}} M_{e,\lambda}(\lambda, T) \cdot A_{bb} \cdot \frac{A_{\det}}{r^2} d\lambda \tag{2.5}$$

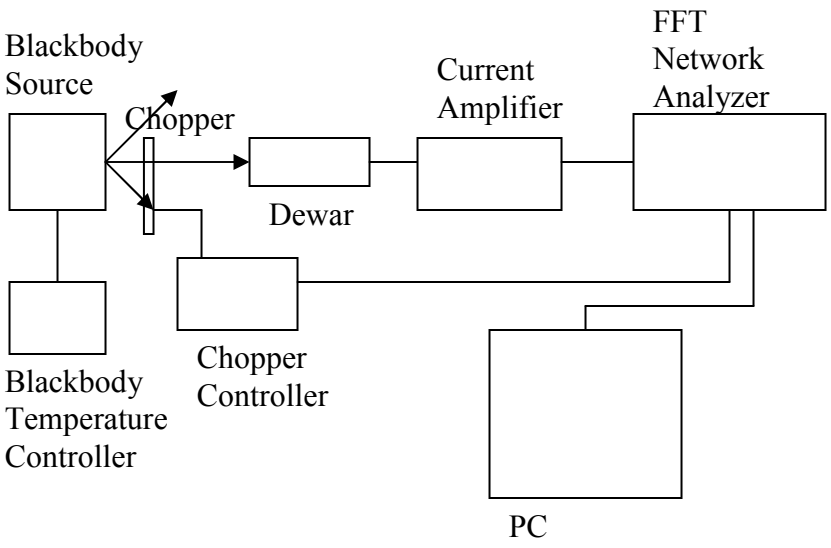

Figure 2.13 Responsivity measurement setup

where M_e is the radiant exitance, A_{bb} is the area of the blackbody aperture, A_{det} is the area of the detector and r is the distance from the blackbody to the detector as shown in Fig. 2.14. The responsivity can then be calculated using the definition of detector responsivity given in Eq. 2.3, the spectral responsivity given in Eq. 2.4 and the estimate for the radiant power from the blackbody incident on the detector given in Eq. 2.5.

$$I(Amps) = \int_0^{\lambda_{cut}} M_{e,\lambda}(\lambda,T)\cdot A_{bb}\cdot\frac{A_{\det}}{r^2}\cdot NR(\lambda)\cdot\Re_{\max}d\lambda \tag{2.6}$$

The solving for the constant R_{max} in Eq. 2.6 gives

$$\Re_{\max} = \frac{I}{A_{bb}\cdot\frac{A_{\det}}{r^2}\int_0^{\lambda_{cut}} M_{e,\lambda}(\lambda,T)\cdot NR(\lambda)d\lambda} \tag{2.7}$$

with units of Amps/Watt.

From equations given in Chapter 1 the detector figures of merit can then be found. From Eq. 1.11 the quantum efficiency as a function of wavelength can be found.

$$\eta(\lambda) = \frac{\Re_{\max} NR(\lambda)}{\lambda} \frac{hc}{q} \tag{2.8}$$

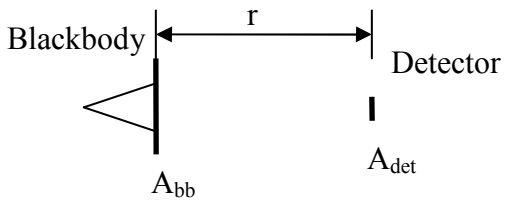

Figure 2.14 Blackbody source and detector configuration for testing

D*(λ) can be found using

$$D^* = \frac{\Re(\lambda)\sqrt{A_d}}{i_n / \sqrt{\Delta f}} \tag{2.9}$$

where i_n is the current noise measured by the spectrum analyzer in the when the blackbody is no longer incident on the detector and Δf is given by

$$\Delta f = \frac{1}{2\tau_{AVG}} \tag{2.10}$$

where τ_{AVG} is the integration time of the measurement.

An alternative approach for measuring responsivity uses a reference detector to estimate the radiometric quantities using the equation

$$A \cdot F \int M_{BB}(\lambda, T) \cdot \Re(\lambda) d\lambda = Signal[Amps] \tag{2.11}$$

where A is the area of the detector (cm), F is a geometrical factor that takes into account the measurement setup geometry, and $M_{BB}(\lambda,T)$ ($W/(cm^2 \cdot \mu m)$) is the spectral excitance

given in equation 1.1. Similar to the above approach using equation 2.11 and rearranging the terms from the integral in equation 2.4 and solving for the constant R_{max}

$$R_{\max} = \frac{Signal}{A \cdot F \int M_{BB}(\lambda, T) \cdot NR(\lambda) d\lambda} \left(\frac{A}{W} \right) \tag{2.12}$$

2.4 Conclusion

In this chapter we discussed the growth, processing and characterization of an InAs/GaSb SL infrared single-pixel detector. Detailed description of characterization techniques used to access the optical and electrical properties of SL detectors was provided. In the next chapter a specific example of an InAs/GaSb SL device will be reported.

3 InAs/GaSb SLS based MWIR detector using nBn design

As stated in Chapter 1, the nBn detector is a new class of infrared photodetector. The concept of the nBn design can be extended to a variety of other material systems. In this chapter we will discuss adapting of the nBn design to InAs/GaSb superlattice.

3.1 Dark current reduction in nBn SL detector

With the exception of our research group, all InAs/GaSb detectors are based on the photodiode design (see table 1.1). At cryogenic operating temperature, the major noise sources for photodiodes are Shockley-Read-Hall (SRH) recombination and surface states. In order to eliminate surface leakage currents different passivation methods have been investigated, such as the deposition of relatively thick layer of dielectric material[42], polyamide passivation[43], overgrowth of wide bandgap material[44], deposition of passivating sulphur coating electrochemically[45] and using ammonium sulfide chemical solutions[46]. All of these methods add complexity to the fabrication and the long term effectiveness is still questionable.

The nBn detector design has been shown to eliminate SRH recombination in bulk semiconductor detectors[37]. Special processing of the nBn detector allows the device to be etched only to the barrier layer and removes the lateral mesa sidewalls.

3.2 nBn Detector Growth

The structures presented in this chapter were grown on n-type Te-doped GaSb (001) substrates by solid source molecular beam epitaxy in a VG-80 reactor equipped with a arsenic valved cracker source, an antimony cracker source and Ga and In SUMO® cells. A detailed description of the growth procedure has been reported elsewhere[39]. The device consists of a 0.35 μm thick n-type superlattice bottom contact layer composed of 8 ML InAs doped with Si (n=4 x 10^{18} cm^{-3}) by 8 ML GaSb followed by the non-intentionally doped (n.i.d.) 1.4 μm thick 8 ML InAs/8 ML GaSb absorber layer. The barrier layer consists of $Al_{0.2}Ga_{0.8}Sb$ with layer thickness of 100 nm. The function of the heterostructure AlGaSb barrier is to block the flow of majority carriers through the device. The barrier composition was chosen so that the majority carrier current (electron current) is blocked while the minority carrier current (hole current) can flow unimpeded because the valence band offset with the surrounding SL layers is minimized. The energy offset in the conduction band is designed and grown to be a thick enough and large enough barrier to prevent electron tunneling from the top contact layer to the absorber layer. The barrier layer is desired to have a zero valence band offset. Due to the complicated nature of SL effective band lineup and the uncertainty involved with SL modeling the exact band offsets are difficult to determine. The best valence band offset and barrier material composition are still being researched. The structure was capped by 100 nm thick top contact layer with the same superlattice composition, thickness and doping concentration as the bottom contact layer. The proceeding structure was grown above an AlGaSb etch stop layer that is used for substrate removal after FPA hybridization.

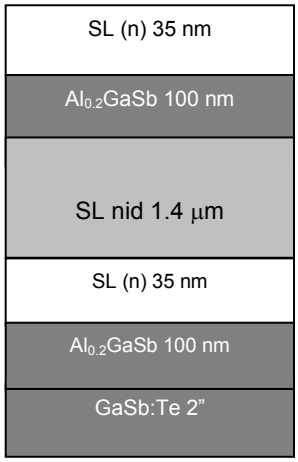

Figure 3.1 Heterostructure schematic of InAs/GaSb SLs MWIR detector after growth

3.3 Contact metallization Study

The nBn structure is designed to operate with n-type layers in flatband or with little depletion. Since SRH generation-recombination current is associated with regions depleted of carriers the heavily doped contact layers required to make ohmic contacts create n-n+ homojunctions. This space-charge region could contribute to the dark current. In order to reduce SRH current, the doping concentration in the contact layer needs to be decreased while still maintaining a good ohmic contact.

To optimize the doping level of the contact layers, several ~ 0.5 μm thick structures consisting of 8 ML InAs doped with Si/8 ML GaSb SL with different doping levels were grown. Doping concentrations as a function of dopant cell (Si) temperature is given in the inset of Fig. 3.2. Transmission line method (TLM) patterns were defined by conventional UV lithography. Metal pads with dimensions of 50 μm x 100 μm spaced from 10 μm to 70 μm apart by increments of 10 μm were used. Commonly used Ti (500 Å)/Pt (500 Å)/Au (3000 Å) metallization was used for the contacts. Samples were

annealed using the following conditions: (I) no annealing (II) 260 °C for 1 minute (III) 350 °C for 1 minute and (IV) 385 °C for 1 minute. Results are summarized in Fig. 3.2. Ti/Pt/Au metallization on undoped SLs material (n=3x10^{16} cm^{-3}) did result in ohmic behavior. Contact resistance was found to be ~55 Ω regardless of annealing temperature.

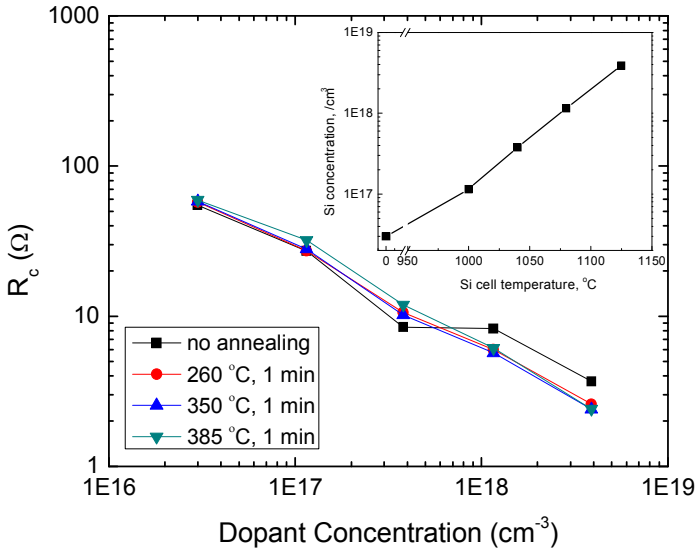

Figure 3.2 Contact resistance versus the doping concentration in the contact layer at different annealing temperatures for Ti/Pt/Au contacts on n-type InAs/GaSb superlattice Inset: The doping concentration as a function of the Si cell temperature

With increasing level of doping concentration in the SL layer, ohmic behavior in the current-voltage characteristics was observed and contact resistance was improved. The structure with the highest doping level (n = 4 x 10^{18} cm^{-3}) demonstrated contact resistance equal to 3.7 Ω (no annealing) and 2.4 Ω (annealing at 350 °C for 1 minute). Annealing at 380 °C did not considerably improve the contact resistance but the surface metal layer was degraded. The results indicate that the doping concentration needs to exceed 1 x 10^{18}

cm^{-3} in order to achieve ohmic contact to n-type InAs/GaSb SLs. In order to obtain ohmic contacts to the InAs/GaSb SL contact layer at lower doping concentration a different metallization needs to be used. GeAu-based metallization on n-type GaSb has been shown to provide good ohmic contact by combining the solid phase reactions of Ge-based contacts with the low ohmic resistance of the Au-based contacts[47]. For the contact resistance study a ~0.5 μm thick 8 ML InAs doped with Si/8 ML GaSb ($n = 5 \times 10^{17}$ cm^{-3}) SL sample was grown. Ge/Au/Pt/Au (287 Å/568 Å/504 Å/2000 Å) contact was deposited then the sample was annealed at 380 °C for 1 minute. TLM measurements revealed contact resistance equal to 1 Ω which indicates that there is good ohmic contact. While this level of contact resistance is desirable the surface quality after annealing is not ideal. Good metal-semiconductor contacts are difficult to achieve with lower semiconductor doping. While there were some promising results from the metal contact study no conclusive result was reached. Therefore the devices presented in this chapter will use highly doped ($n=4 \times 10^{18}$ cm^{-3}) contact layers with Ti (500 Å)/Pt (500 Å)/Au (3000 Å) metallization. Since the post-annealing contact resistance improved by a factor of 1.5, the heat treatment of the contacts was omitted.

3.4 nBn Detector Device Processing

The devices were processed into two distinct structures (referred to as structure A and structure B) using 410 μm x 410 μm square mesas with circular apertures ranging from 25 μm to 300 μm. Processing was initiated by standard optical photolithography for top contact metal deposition. Ti (500 Å)/Pt (500 Å)/Au (3000 Å) was used for both top and bottom contact metallization. Structure A was etched using H_3PO_4:H_2O_2:H_2O solution

with a ratio of (1:2:20) to the middle of the barrier layer (etch depth ~ 0.15 nm). Then both structures A and B were inductively coupled plasma dry etched to the middle of the bottom contact layer. The bottom contacts for structure A were significantly far away from the top contact so that the etched sidewall surface current would not contribute to the device current. Both samples were then patterned and bottom contact metal was deposited. Schematics of structures A and B are shown in Fig. 3.3 and Fig. 3.4 respectively.

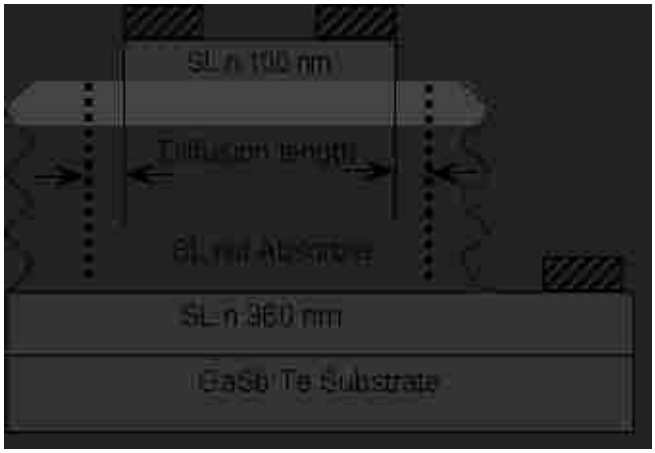

Figure 3.3 Schematic of structure A (shallow etch)

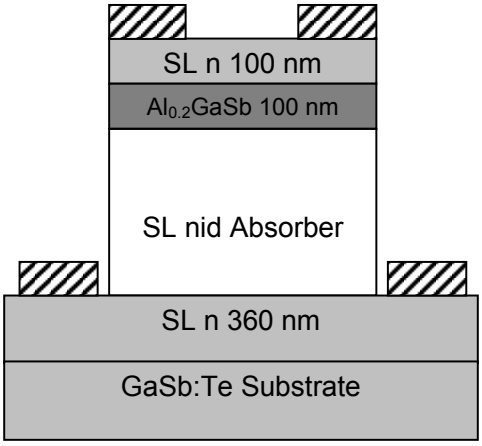

Figure 3.4 Schematic of structure B (deep etch)

For structure A the active area of the device is defined by the diffusion length of the minority carriers (holes) rather than by a conventional mesa. For structure B dangling bonds are present on the etched mesa sidewalls and surface leakage current is expected to be high.

3.5 nBn Detector Device Characterization

After processing, the devices were cleaved then mounted and wire bonded to a leadless chip carrier (LCC) for characterization. Current voltage characteristics were measured in the range 77K - 293K range with the detector facing a cold shield using a HP4145 Semiconductor Parameter Analyzer. In this work the forward bias of an nBn detector is defined as a positive voltage applied to the bottom contact of the detector. The dark current densities measured at V = 0.1V for structures A and B as a function of temperature are shown in Fig. 3.5 and the dark current densities as a function of applied voltage is given in Fig. 3.6.

The ratio of dark current densities measured at the same value of applied bias is also shown. At high temperature the thermally generated carriers dominate the dark current and the influence of the surface current is not seen because of the large size of the mesa. The bulk component of dark current is strongly temperature dependent so as the temperature decreases the surface current becomes the dominant component of dark current at low temperature. The levels of dark current in structures A and B are comparable at 250 K but the dark current in structure A is reduced by two orders of magnitude at 77 K. Dark current densities were equal to 2.3×10^{-6} A/cm^2 and 3.1×10^{-4}

A/cm^2 for structures A and B respectively at V_b = 0.1V and T = 77K. At 250K, the dark current density was equal to ~ 80 mA/cm^2.

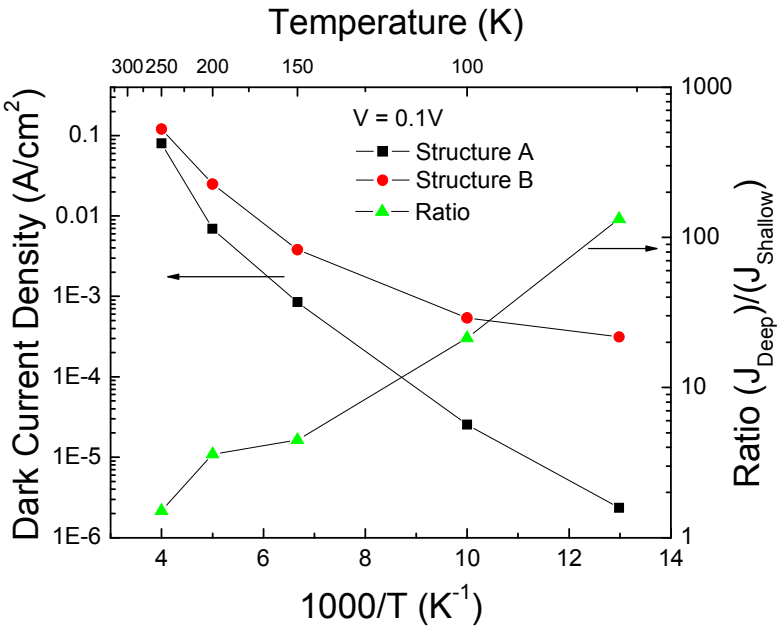

Figure 3.5 The dark current density vs. 1000/T in structures A (shallow etched) and B (deep etched) (V_b = 0.1V). Right Axis: Ratio of dark current densities for both structures

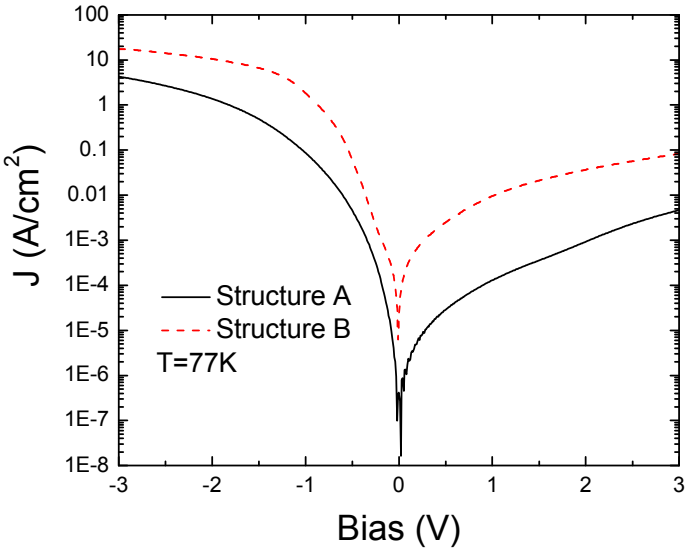

Figure 3.6 Current Density vs. Voltage for structures A (shallow etched) and B (deep eteched) at 77 K

To confirm that the surface current is reduced measurements were undertaken at industrial collaborators Santa Barbara Focal Plane (SBFP). The samples were hybridized to a silicon fanout using compression indium bump bonds. To separate the surface and bulk contributions to the current, dark current measurements were performed using Variable Area Diode Array (VADA) with device size varying from 270 μm to 30 μm. The surface leakage current is due to the mesa sidewalls so as the ratio of perimeter to area (P/A) increases the contribution of the surface leakage current increases. To show that the majority of the current is flowing through the bulk of the semiconductor, there should be little change in the current density as the P/A increases. The current density is chosen since its square root is proportional to the limiting Shot Noise contribution. The current density vs. P/A as shown in Fig. 3.7 is not always completely flat as might be

expected with complete passivation. This could be due to lateral collection because the devices do not have physically defined areas the devices are collecting carriers from the surrounding area. The lateral collection would present itself in a similar way as surface current, as the size of the device decreases and the lateral collection stays the same the ratio of the device current to the lateral collection would increase. Also, the processed devices still have exposed sidewalls which can contribute to the dark current. For complete analysis of the elimination of the surface leakage currents, a comparison of deep and shallow etched VADA at different temperatures must be performed.

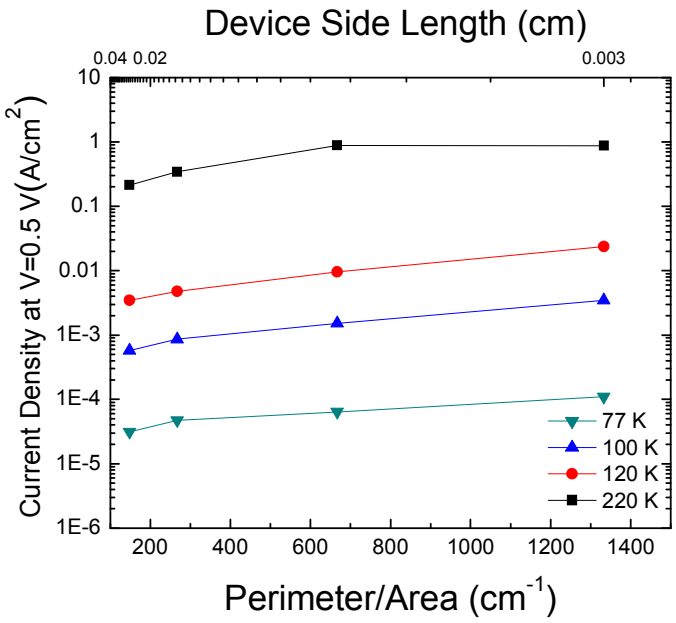

Figure 3.7 Current density vs. Perimeter/Area at V = 0.5V performed by Santa Barbara Focal Plane

Temperature dependent spectral response of structure A was measured using a Nicolet 6700 Fourier Transform Infrared (FTIR) Spectrometer from 77K – 250K. The spectral response was seen all the way up to 250K (V_b=0.5V). The cut-off wavelength shifted

from ~ 4.2 μm at 77K to ~4.8 μm at 250K. The responsivity and quantum efficiency (QE) were measured for structure A as shown in Fig. 3.7.

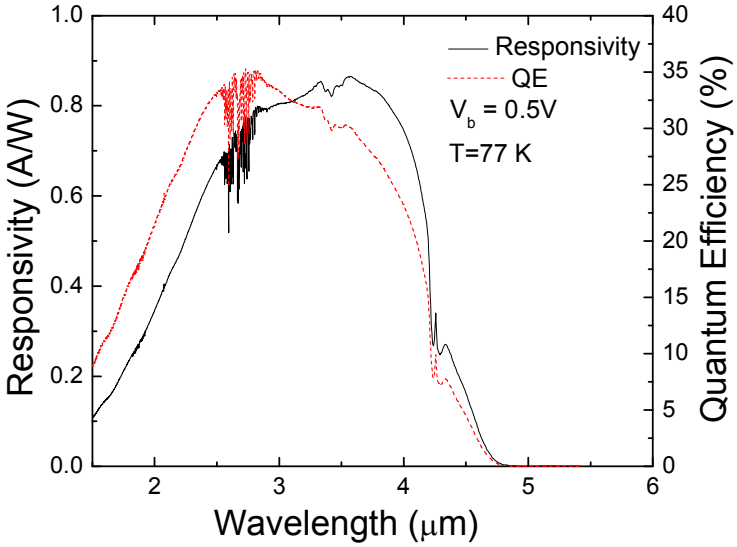

Figure 3.8 The responsivity (solid black line, left axis) and quantum efficiency (dotted red line, right axis) for structure A (shallow etch)

For the responsivity measurement, the device was placed in a pour-fill dewar and cooled with liquid nitrogen. The peak responsivity was calculated using a calibrated Micron blackbody source at 500K. The signal was collected using a Stanford Research Systems Model SR570 Low-Noise Current Preamplifier and Model SR770 FFT Network Analyzer. The peak responsivity is then calculated using the normalized spectral response and the peak black body response. For structure A the peak responsivity was found to be 0.835 A/W at 3.5 μm with V_b = 0.5V. The responsivity and QE at 4 μm was 0.74 A/W and 23% respectively. No Antireflection (AR) coating was applied on the device.

The spectral specific detectivity D*(λ) was estimated using

$$D^* = \frac{\Re(\lambda)}{\sqrt{2qJ(V) + \frac{4kT}{R_d A_d}}} \tag{3.1}$$

where R(λ) is the spectral responsivity, and 2qJ(V) estimates the shot noise and $4kT/R_dA_d$ estimates the Johnson noise at a given voltage. Peak D* was estimated to be 2.8 x 10^{11} cm $Hz^{1/2}$/W at 4 μm at V_b = 0.5 V.

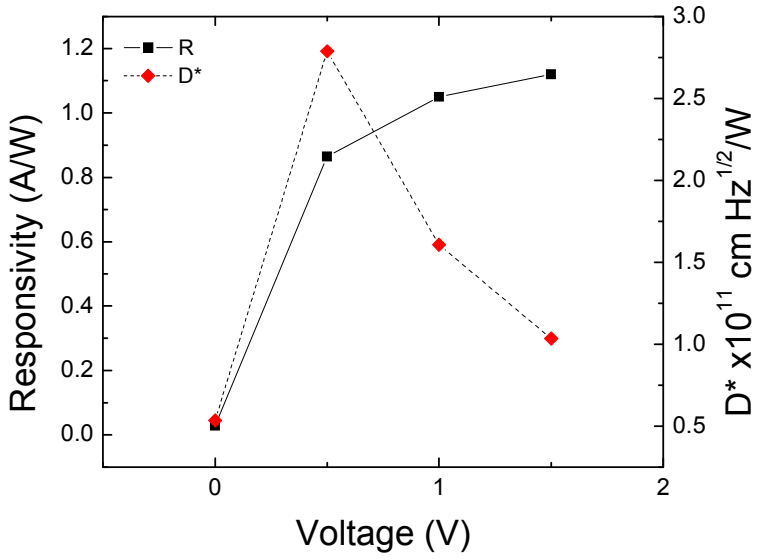

Figure 3.9 Peak Responsivity and D* as a function of applied bias for structure A (shallow etch)

3.6 Superlattice nBn 320 x 256 Focal Plane Array

In collaboration with QmagiQ LLC, we produced a 320 x 256 InAs/GaSb superlattice nBn focal plane array. The SEM image in Fig. 3.10 shows the shallow etched top contacts and deep etched bottom contacts performed at CHTM. The noise equivalent temperature difference (NETD) is given in Fig. 3.11. The mean NETD was 23.8 mK at 77 K for an integration time of 16.3 ms using f/4 optics. Fig. 3.12 is a thermal image

taken with the 320 x 256 InAs/GaSB superlattice nBn camera with detector temperature at 77 K and an integration time of 16.3 ms, a two-point non-uniformity correction was utilized.

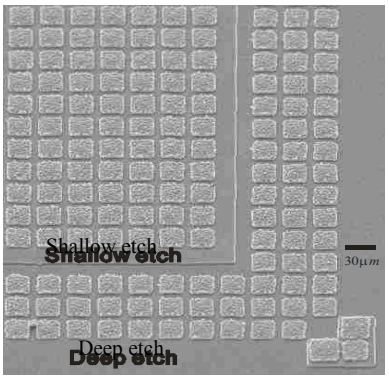

Figure 3.10 Scanning Electron Microscope (SEM) image showing part of a fully processed Focal Plane Array with a shallow etched top contacts and deep etched bottom contacts with indium bumps

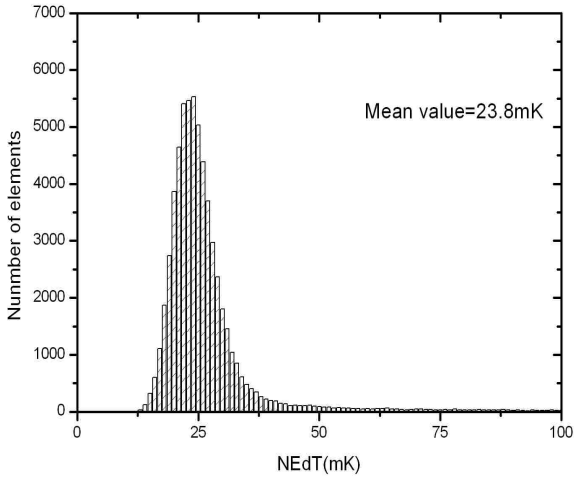

Figure 3.11 The Noise Equivalent Temperature Difference (NETD) distribution in the FPA for an integration time of 16.3 ms using f/4 optics

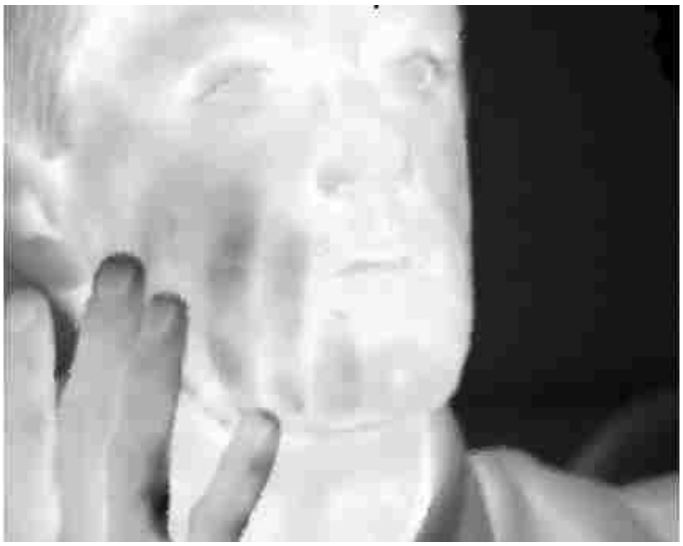

Figure 3.12 Thermal image taken with at 77 K with and integration time of 16.3 ms and using a two-point non-uniformity corretction

3.7 Conclusion

In this chapter, we discussed high performance nBn detector based on InAs/GaSb SL with a cut-off wavelength of ~ 4.8 μm at 250K. Due to the way the device was defined and processed, low temperature dark current was reduced by two orders of magnitude due to elimination of surface currents in comparison with conventional photodiode processing. Dark current densities were equal to 2.3 x 10^{-6} A/cm^2 and 3.1 x 10^{-4} A/cm^2 for detectors with shallow etch defined mesa (structure A) and conventionally defined mesa (structure B), respectively. At 250K the dark current density was ~ 80 mA/cm^2 for both devices. VADA measurements revealed that the surface current does not increase linearly with the increase of the P/A ratio. Comparison of conventional mesa etched and shallow isolation etched VADA current density at operational temperature would clearly show whether the surface currents were eliminated. Removal of surface leakage currents is important for

fabrication of high performance focal plane arrays (FPAs) based on InAs/GaSb SL operating in MWIR.

4 InAs/GaInSb SLS based detector using nBn design with 8 μm cutoff

In this chapter we discuss the implementation of InAs/GaInSb strain-layer superlattice detectors with cutoff wavelength of 8 μm. The motivation for why surface leakage current is the limiting factor in development of large area LWIR photodetector FPAs is discussed. Then growth, processing and characterization of an 8 μm cutoff InAs/GaInSb nBn detector much is detailed much like as in chapter 3. IV characteristics of the nBn detector are compared with a PIN photodiode with the same absorber region structure. The nBn exhibits significantly lower current density than the PIN diode at equivalent applied electric field. The special processing of the nBn detector and the removal of the sidewall surface is effective regardless of the increase in the cutoff wavelength of the detector.

4.1 Surface leakage current in InAs/GaSb LWIR

The surface leakage current of low bandgap devices increases when the bandgap of the device is lowered. Most of the surface leakage is due to tunneling of electrons. In most higher bandgap (> 1 eV) III-V devices, dielectric materials like silicon dioxide or silicon nitride are used for passivation. The interaction between the insulator-semiconductor interface affects the Fermi level at the boundary of the device by electrostatic interaction and can cause band bending of ~ 10 meV. For narrow bandgap semiconductors like the 120 meV bandgap corresponding to 10 μm cutoff band bending caused by interface states results in a strong increase of surface tunneling currents[44].

4.2 Growth and Processing

The structures presented in this chapter were grown on n-type Te-doped GaSb (001) substrates by solid source molecular beam epitaxy in a VG-80 reactor equipped with a arsenic valved cracker source, an antimony cracker source and Ga and In SUMO® cells. Two separate devices were grown an nBn detector and a PIN detector in subsequent growth runs. The schematic structures are shown in Fig. 4.1. The nBn device (sample A) consists of a 0.35 μm thick n-type superlattice bottom contact layer composed of 8 ML InAs doped with Si (n=4 x 10^{18} cm^{-3}) by 8 ML GaSb followed by the non-intentionally doped (n.i.d.) 2.35 μm thick 9 ML InAs/5 ML $Ga_{0.75}In_{0.25}Sb$ absorber layer. The absorber superlattice period structure was taken from Ref. 44 and the expected cutoff wavelength was 10 μm at 77 K. The barrier layer consists of $Al_{0.2}Ga_{0.8}Sb$ with layer thickness of 100 nm. A barrier that gives zero valence band offset for this superlattice structure is under experimental and theoretical examination in our group. The structure was capped by 100 nm thick top contact layer with the same superlattice composition and doping concentration as the bottom contact layer.

The PIN device (sample B) consists of 15 periods of 8 ML InAs:Si/8 ML GaSb SL bottom contact layer then 15 periods 9 ML InAs:Si/5 ML GaInSb for the n-type layer. The absorber layer shares the same size and growth as the absorber for the nBn and is 2.35 μm thick n.i.d. 9 ML InAs/5 ML GaInSb. The p-type side is 15 periods InAs/GaInSb:Be and is capped by a 100 μm GaSb:Be top contact layer.

The nBn device was processed using the standard optical photolithography and the devices were defined with a shallow isolation etch as described in chapter 3. The PIN device was processed into a conventional mesa structure as defined in chapter 2. Both

samples A and B were not passivated so that the effect of the surface current would be evident.

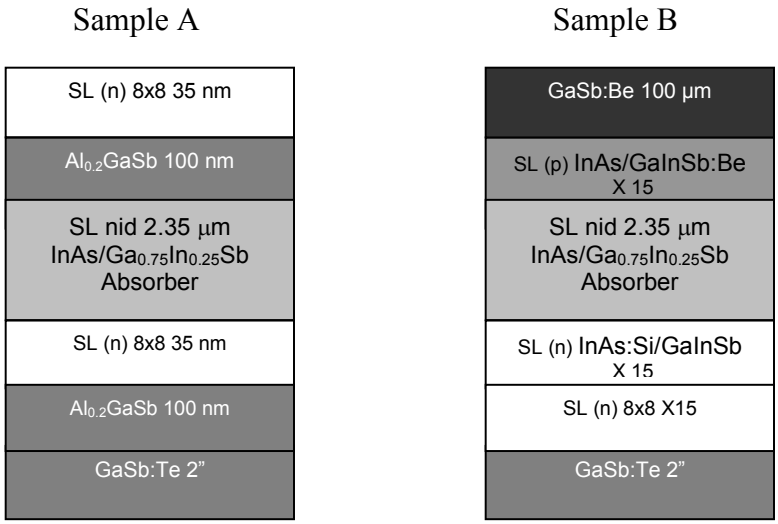

Figure 4.1 Schematic structure of nBn (Sample A) and PIN (Sample B) 8 μm λ_{cutoff} detectors

4.3 Device characterization and comparison

After processing the samples were individually wire bonded to an LCC and mounted in a cryostat as described in Chapter 3. Temperature dependent IV characteristics with room temperature background illumination were performed for samples A and B and are shown in Fig 4.2 and Fig. 4.3 and are compared on the same graphs in Fig. 4.4. The current density at 0.2V is 6.24 x 10^{-5} A/cm^2 for the nBn and for the PIN at -0.2V is 1.03 A/cm^2 both at T = 77 K as shown in Fig. 4.5. While both devices were not optimized, the nBn device exhibited lower current density while the PIN is dominated by a large noise current. The significantly lower current density for the nBn detector compared to the PIN diode can be attributed to both the efficiency of the device structure and the special processing that removes the effect of the surface currents. Enough though the PIN device

is by no means comparable to published state of the art detectors at this cutoff wavelength, the fact that both samples were grown in consecutive growth runs and was processed in the same clean room at the same time show the advantages provided by the nBn device.

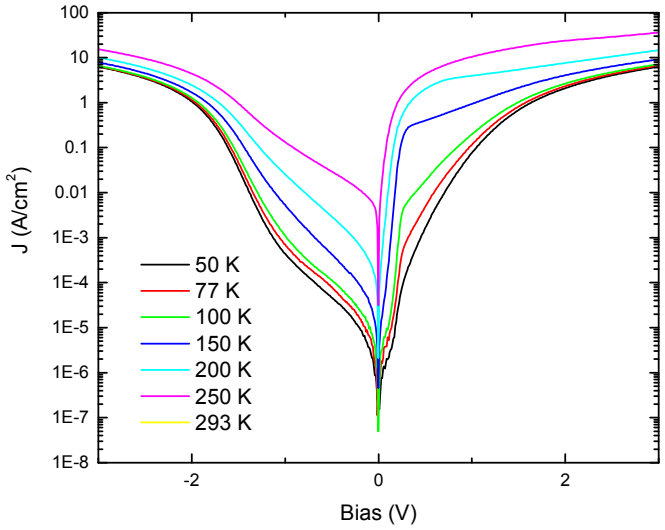

Figure 4.2 Room temperature background JV plotted at different temperatures for sample A (nBn)

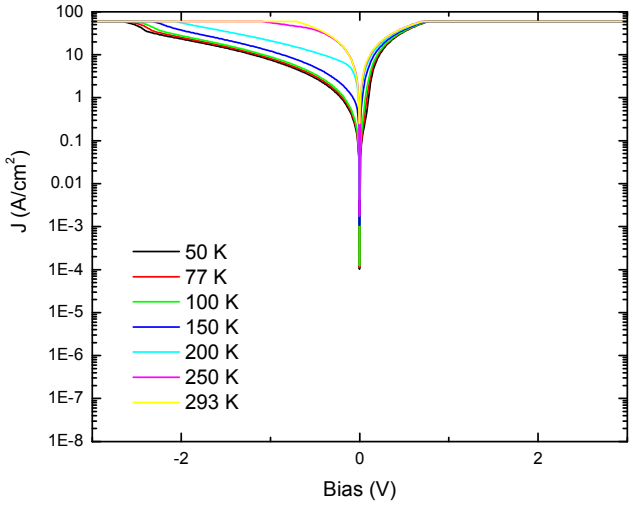

Figure 4.3 Room temperature background JV plotted at different temperatures for sample B (PIN)

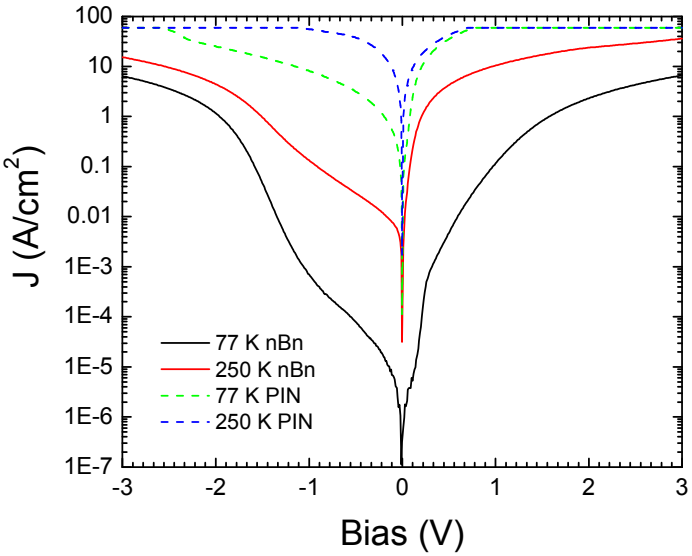

Figure 4.4 Comparison of sample A (nBn) and B (PIN) current density as a function of applied bias at T = 77 K and 250 K

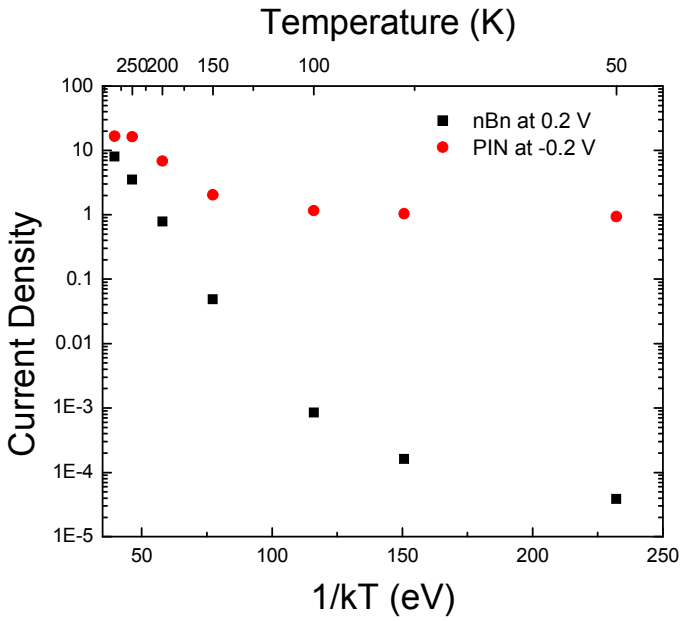

Figure 4.5 The current density for sample A (nBn, black) and B (PIN, red) versus 1/kT

The spectral response of both devices is given in Fig. 4.6 and Fig. 4.7. The bias for the nBn device is V_b = 0.2 V while the PIN device spectral response is given at zero bias (V_b = 0V) V. The SNR at 77 K is slightly better for the nBn device. At 150 K the SNR of the PIN device is significantly degraded compared to the nBn SNR response.

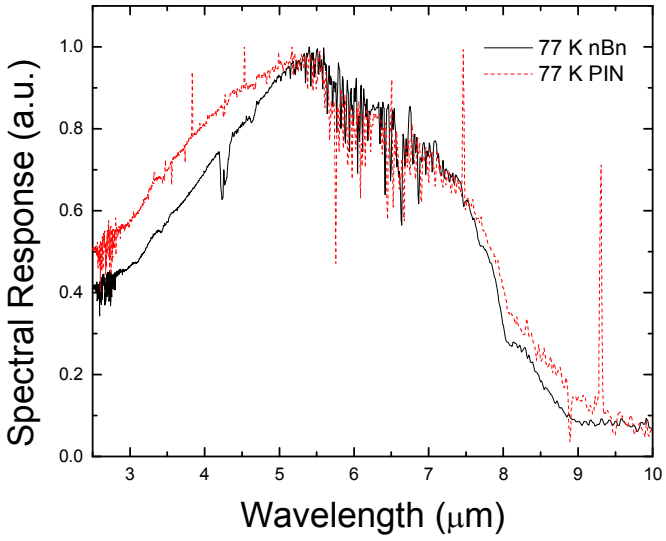

Figure 4.6 Normalized spectral response of samples A (nBn, black) and B (PIN, red) at 77 K

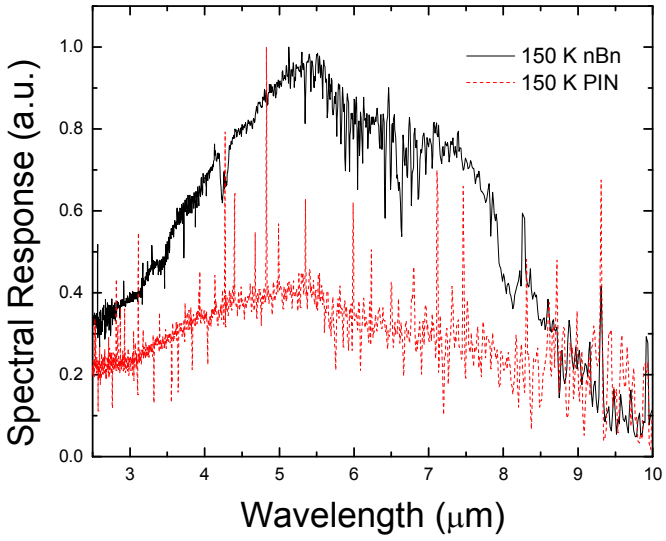

Figure 4.7 Normalized spectral response of samples A (nBn, black) and B (PIN, red) at 150 K

The responsivity and quantum efficiency were measured for sample A using the same setup as in Chapter 3. The external quantum efficiency was calculated to be 12% and D*

was calculated to be 2.5 x 10^{10} cm $Hz^{1/2}$/W at 5.5 μm. The peak responsivity was 0.51 A/W also at 5.5 μm. The responsivity and quantum efficiency is shown in Fig. 4.6. One possible explanation for the relatively low quantum efficiency could be the poor alignment of the valence band of the barrier with the 9 ML InAs/5 ML $Ga_{0.75}In_{0.25}Sb$ SL.

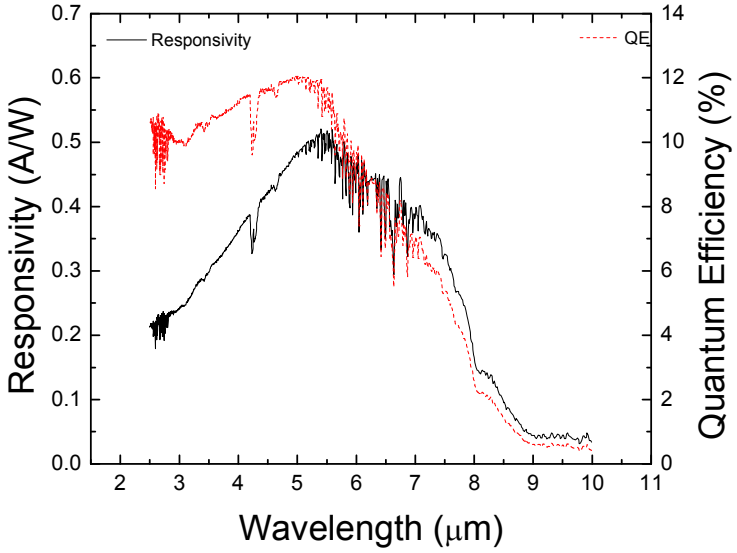

Figure 4.8 Responsivity (left axis, black line) and Quantum Efficiency (right axis, red line) are given as a function of wavelength for sample A (nBn)

Atmospheric absorbance above 5 μm to 8 μm limits the response of the detector. Further study is currently underway on different superlattice period composition that will increase the cutoff wavelength. A similar study of PIN and nBn devices using the new superlattice absorber region is currently under investigation in our group. The barrier material and composition is also currently being studied on 8x8 SL devices. Ref. 32 suggests that the valence energy level in standard type II superlattice stays almost the same regardless of superlattice design. While our own theoretical analysis is underway,

this could mean that if an ideal barrier could be found, it could be used in any standard type II superlattice structure with little optimization.

4.4 Conclusion

In this chapter we showed an nBn detector with 8 μm cutoff. The nBn device was compared to a PIN device with the same λ_{cutoff}. The lower current density of the nBn device shows the advantages of the device structure. While these results are promising, the low quantum efficiency of the device must be improved if this material is to be made into an FPA.

5 Conclusions and Future Work

5.1 Conclusions

This main focus of this paper is to introduce InAs/GaSb SL nBn detectors as a way to increase the performance of SL detectors and to utilize the following advantages of the material system. InAs/GaSb SL has high responsivity because of strong absorption of normal incidence photons. Larger electron effective masses that are not directly dependent on the bandgap energy lower the tunneling current compared with bulk materials with the same bandgap energy. Different combinations of superlattice periodicity or constituent material composition can be utilized to tune the superlattice bandgap which can be used to provide multicolor capability. Also, the light-hole and heavy-hole band separation can be adjusted to reduce Auger recombination.

In chapter 1 of this thesis we introduced the general concept of infrared detection and distinguished between two different classes of IR detectors, thermal and photon detectors. Photon detectors were further split up into either photoconductive or photovoltaic detectors. Traditional detector figures of merit responsivity, noise equivalent power and specific detectivity and their theoretical limits were discussed. The strengths and weaknesses of existing FPA technology were briefly discussed. InAs/GaSb based detectors were covered as a possible alternative to existing FPA technology. Finally nBn detectors were introduced.

In chapter 2 the growth, processing and optical and electrical characterization of InAs/GaSb IR detectors was explained. Material growth using solid source molecular

beam epitaxy was briefly explained. Processing of a single-pixel device was also briefly covered. The optical and electrical characterization of the devices section included the explanation of temperature dependent IV measurements, spectral response measurements using a FTIR spectrometer and the responsivity measurement setup.

In chapter 3 the growth, processing and characterization of an InAs/GaSb SL nBn detector with a cutoff wavelength of ~ 4.25μm at 77 K was given. Two structures were fabricated out of the same growth material, one with a shallow top contact isolation etch (structure A) and one with a conventional mesa structure (structure B). The shallow etched device dark current was reduced by two orders of magnitude at 77 K compared with the deep etched device. The current density was equal to 2.3 x 10^{-6} A/cm^2 for and 3.1 x 10^{-4} A/cm^2 for structures A and B respectively at V_b = 0.1V and T = 77K. At 250K, the dark current density was equal to ~ 80 mA/cm^2. The responsivity and QE of structure A were measured at 4 μm to be 0.74 A/W and 23% respectively.

In chapter 4 we compared the electrical properties of an nBn detector and a PIN detector with the same absorber thickness and structure (λ_{cutoff} = 8 μm) from subsequent growth runs. The current density at 0.2V is 6.24 x 10^{-5} A/cm^2 for the nBn and for the PIN at -0.2V is 1.03 A/cm^2 both at T = 77 K. While the growth for neither device was optimized, the large difference between the devices shows that the nBn detector structure provides significant advantages in the electrical properties (lower dark current) which we expect to carry over into the optical properties (better signal to noise ratio) of the device. While the responsivity of the nBn detector was low, 0.51 A/W at 5.5 μm, the expectation is that this will be increased in future devices.

In conclusion, we showed that the nBn detector can be extended to InAs/Ga(In)Sb superlattice material. Shallow etching of the devices lowered the dark current at lower temperatures by removing the surface current component. nBn detectors with λ_{cutoff} of 4.25 and 8 μm at 77 K were demonstrated.

5.2 Future Work

nBn InAs/GaSb superlattice detectors show promise for increasing the performance of SL FPAs. Questions behind the physics of this material system still remain unsolved. The integration of the nBn detector design raises even more questions on the physical mechanisms behind detection. There are still many topics for future research with these devices.

5.2.1 Lateral Collection

The issue of lateral collection due to in-plane carriers in the shallow etched devices needs to be thoroughly investigated. Preliminary investigations by our industrial collaborators Santa Barbara Focal Plane show that there is that lateral collection of 20 to 60 μm in measured devices. The lateral collection is a significant issue when incorporating this material into a FPA where one square pixel has a side length of ~25 μm and the pitch is ~30 μm. Optical and electrical crosstalk would then limit the performance of the FPA. A trade off exists then between defining devices with a shallow isolation etch to remove the surface leakage currents and the amount of crosstalk that will can be tolerated in the FPA. Studies of superlattice in-plane mobility have been preformed by L. Faraone group in Western Australia using quantitative mobility spectrum analysis (QMSA) [48] on

conductive GaSb substrates. Further work is being performed on the mobility in the growth direction. Better understanding of the in-plane and growth mobility could allow for optimization of the superlattice material in an attempt to lower the lateral collection in the devices. Additionally, research into the minority carrier diffusion length and minority carrier lifetime in superlattice material could be incorporated in improving nBn detector performance.

5.2.2 nBn theoretical modeling

The theory behind the nBn detector is by no means fully understood. Theoretical modeling of InAs with InAsSb barrier nBn detectors could provide insight that could be helpful in understanding InAs/GaSb SL nBn detectors. For superlattice simulation current techniques used in our research group for modeling of InAs/GaSb superlattice provide useful information about the expected cutoff wavelength, separation of the conduction and valence bands and expected wavefunctions for the electrons and holes. Information that is not currently available is the position of the conduction and valence bands with respect to a reference level. The alignment of the barrier to the first valence band in InAs/GaSb is critical to the operation of the nBn detector, so the position of the conduction and valence levels to a reference level could provide insight as to what barriers could be used. While experimental barrier composition studies are underway, further study incorporating theoretical SL data into nBn device modeling will be crucial in understanding the physics behind the nBn detector.

5.2.3 Focal Plane Array Fabrication

The ultimate goal of this research is to make the nBn detector into a Focal Plane Array (FPA) that can be hybridized to a read-out integrated circuit (ROIC). The first InAs/GaSb SL nBn detector based FPA has been with made with collaboration from QmagiQ LLC.

Figure 5.1 MWIR image captured from the first SL nBn FPA with a non-uniformity correction applied at T = 77 K with a NETD = 26mK

Future FPA will be hybridized at The University of New Mexico at The Center for High Technology Materials. This will allow both MWIR and LWIR SL nBn detectors to be hybridized onsite. This technology can also be used to hybridize fanout circuits to ROICs so that small area single pixel devices that are too small to consistently wire-bond

(< 100 μm). The fanout could then be used for temperature dependent measurement of VADA IV.

5.2.4 Multispectral nBn devices

Multicolor nBn detectors have been demonstrated using nBn SL detectors[36], but are still just single pixel devices. Unlike other InAs/GaSb SL multispectral detectors that require two In bumps per pixel and custom designed ROIC[49], the multispectral nBn cutoff wavelength would be bias dependent. The processing steps for conventional FPAs would not need to be modified and off the shelf ROICs could be used.

5.2.5 Multiple barrier devices

Recent research has shown that 10 μm cutoff can be achieved while measuring the spectral response with a bias applied across two top contacts. While the mechanism of detection is not fully understood, the only material with 9 μm cutoff is in the absorber layer meaning that the material is truly absorbing. More research needs to be done both experimentally and theoretically to understand the physics behind this.

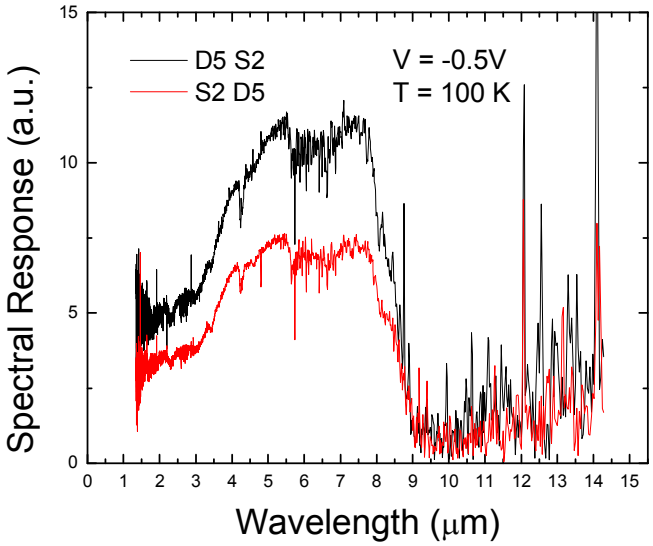

Figure 5.2 Spectral response of nBn detectors with a bias V_b = -0.5V across two top contacts at T = 100 K

Appendix A

Processing steps for nBn_L8_11_12_13_14_SLS

1. Mesa Shallow etching	1.1. Wafer clean	Acetone/Methanol/DI rinse (5 minute each) Nitrogen dry 6 minute dehydration bake @ 150°C
	1.2. Photolithography	Mask: mesa etch—positive PR HMDS, 5k rpm, 30 sec 150°C / 30 sec AZp4330, 5k rpm, 30 sec, 90°C / 90 sec Mask Exposure time = 11 sec, CI2 setting Develop AZ 400k (1:4), time ~70 sec(????)
	1.3 Dry Etching	ICP, Gas : BCl_3, Recipe : Zia-InP ICP power : 500W, RF power : 80W Etch time (40~45SEC.) (Etch rate : ~4.5nm/Sec and after 5 min each rate might differ with time)
	1.4 Wet Etching 1.5 PR removal	H202:H3PO4:H2O=2:1:20 For 30 sec to 1min PR removal using Acetone or RIE cleaning
	1.6. Quality control	Inspect etch pattern with alfa-step.

Appendix A

2.Mesa Deep etching	2.1. Photolithography	Acetone/Methanol/DI rinse (5 minute each) Nitrogen dry 6 minute dehydration bake @ 150°C
	2.2. Photolithography	Mask: passivation—positive PR HMDS, 5k rpm, 30 sec 150°C / 30 sec AZp4330, 4k rpm, 30 sec, 90°C / 90 sec Mask Exposure time = 11 sec, CI2 setting Develop AZ 400k (1:4), time ~70 sec(????)
	2.3 Etching	ICP, Gas : BCl_3, Recipe : Zia-InP ICP power : 500W, RF power : 80W Etch time (??) (Etch rate : ~2600 Å/min and after 5 min each rate might differ with time)
	2.4 PR removal	PR removal using Acetone or RIE cleaning
	2.5. Quality control	Inspect etch pattern with alfa-step.
3. Top and bottom metal deposition	3.1. Wafer clean	Acetone/Methanol/DI rinse (5 minute each) Nitrogen dry 6 minute dehydration bake @ 150°C

	3.2. Photolithography	Mask: cmetal—negative PR HMDS, 5k rpm, 30 sec 150°C / 30 sec AZ5214E-IR, 5k rpm, 30 sec~45Sec 90°C / 90 sec Mask Exposure time = 3.5 sec, CI2 setting 112°C / 60 sec (image reverse bake) Flood exposure time = 60 sec, CI2 setting Develop AZ400K 1:5, DI water, time = ~45 sec
	3.3. Metal deposition	Ti : 500 Å @ 2Å /sec Pt : 500Å @ 1 Å /sec Au: 3,000 Å @ 2.5 Å /sec
	3.4. Life -off	Acetone, Over 10 minute. Acetone spary.
	3.5 Quality control	Inspect patterns using microscope

Appendix B

Background Correction Instructions

Part 1

Explanation

The DTGS is a pryoelectric detector. The DTGS detector measures the power output from the IR source inside the FTIR. The response of the DTGS is not independent of frequency. As the frequency increases the magnitude of the response decreases. To correct for this, the response of the DTGS was measured using a 980 nm diode laser in the frequency range 400 Hz to 10 kHz. Using $f = n\nu$ where f is the frequency, n is the wavenumber and ν is the velocity, correction curves were plotted for the wavenumber range 7400 – 400 cm^{-1}. Higher velocities match the wavenumber range of the DTGS better.

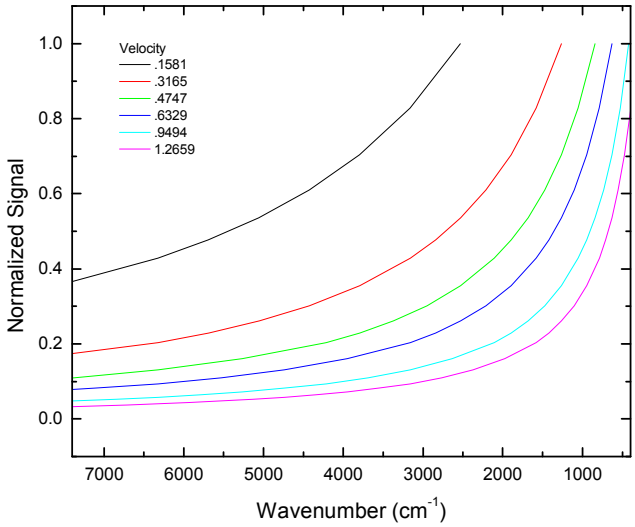

Figure App. B. 1

1. Mount and cool device either as explained in **Cryogenic Spectral Response Measurements using FTIR** in lab 175A or in a pour-fill dewar in the MICA lab.

2. Open OMNIC application. 

3. Open the **Experiment Setup** under the **Collect** tab or press Ctrl-E.

4. In the **Experiment Setup** window under the Collect tab choose the final format as SingleBeam.

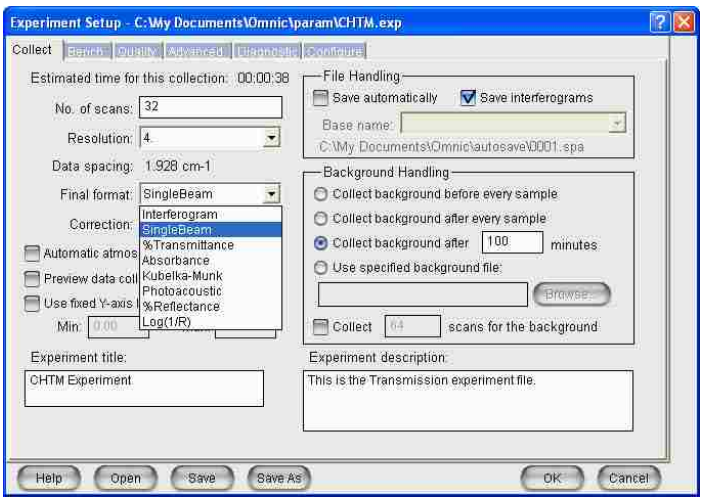

Figure App. B. 2

5. Under the Bench tab in the **Experiment Setup** window verify that the settings for the sample compartment is Main, the Detector is **DTGS TEC**, the Beamsplitter is **XT-KBr**, the source is **IR**, and the proper accessory is selected. Set the gain to **one (1.0)** and select a velocity from the Velocity drop down menu as shown in Figure 2. The Max and Min (top left circled in red) values should be in the range –10 to 10 otherwise the measurement will saturate. Also, the lower the velocity the smaller the Aperture should be.

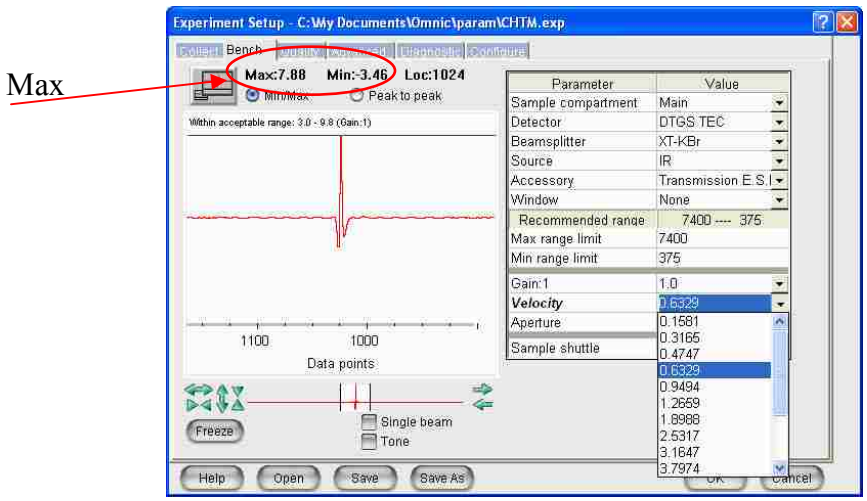

Figure App. B. 3

6. Under the advance tab in the **Experiment Setup** window set the Phase Correction drop down menu to Power Spectrum. Power Spectrum is used to prevent negative values during spectral response measurements.

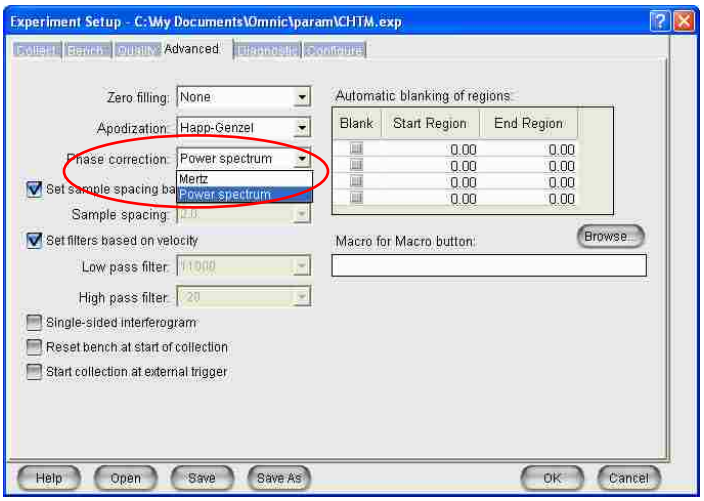

Figure App. B. 4

7. Open the sample compartment on the FTIR to let in the Atmosphere then Collect the background spectrum. The sample compartment has a nitrogen purge that removes the atmospheric interference from H_20 and CO_2. Opening the sample compartment reintroduces the atmospheric interference to the DTGS detector. Since the sample to

be measured is outside the FTIR this helps approximate the atmospheric interference from the IR source to the sample detector.

8. Save the collected background by clicking File then save or press F12.
9. Open the correction curve for the Velocity of the background spectrum by choosing .csv text as the type of file and matching the file name to the velocity chosen in step 5. In Figure 2 the velocity was set at .6329. To match that open the .csv file .6329. C:\My Documents\OMNIC\Spectra\Velocity Correction Curves

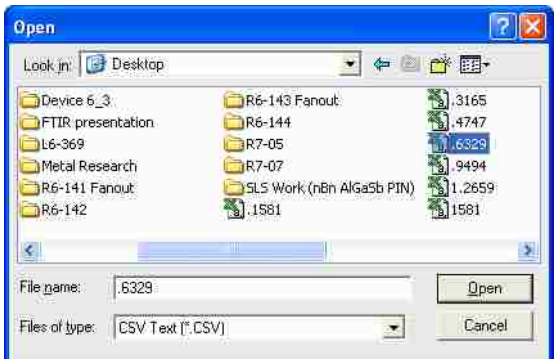

Figure App. B. 5

10. Set the parameters Y units to **Single beam** and the resolution to match the resolution of the background measurement and press OK.

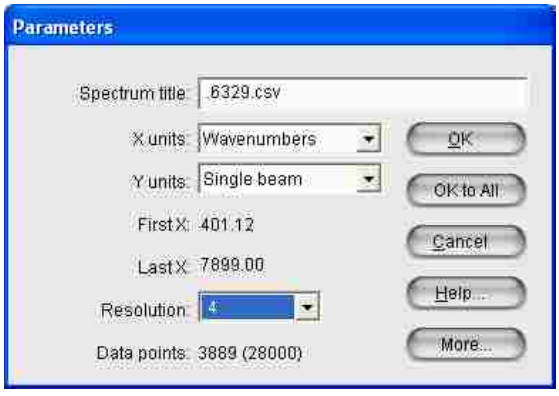

Figure App. B. 6

11. In the OMNIC window, first select the background curve then select the correction curve. The order of the selection is important 1) background 2) correction. To do this first click on the uncorrected background spectrum, the line should be red. Next hold down **Ctrl** and click the correction curve. Both lines should be red.

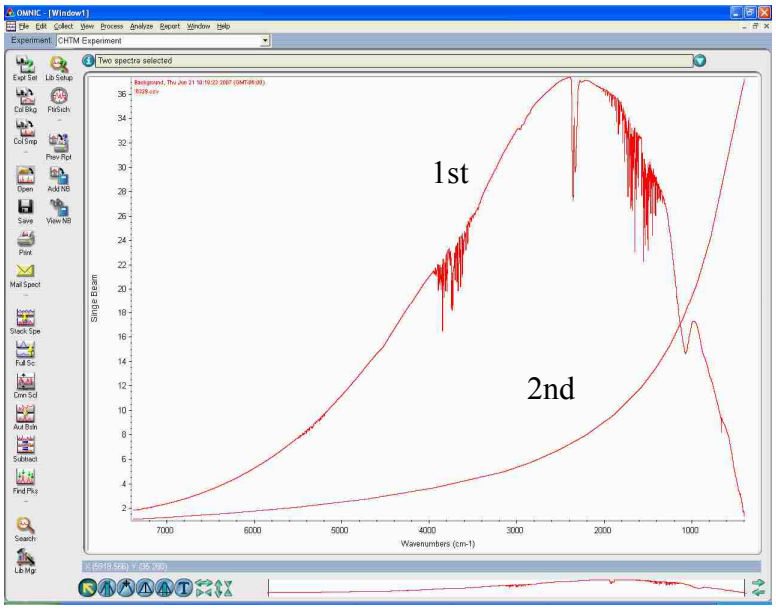

Figure App. B. 7

12. With both lines highlighted red click on the Process tab and select **Spectral Math…**
13. In the operation drop down menu select A / B. A is the background file, B is the correction curve.

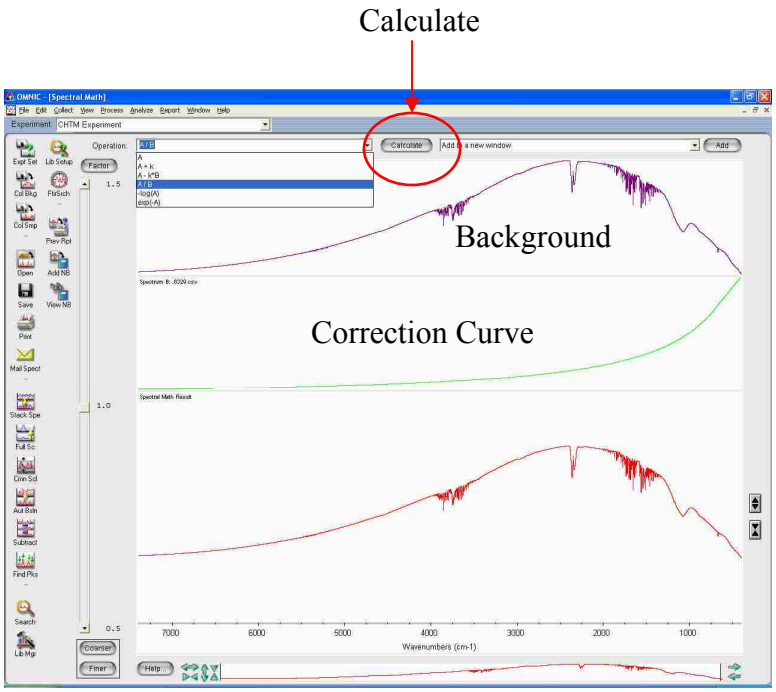

Figure App. B. 8

14. Press the Calculate button next to the Operation menu.

15. Add the result to the desired window by selecting the window number or Add to a new window in the drop down menu.

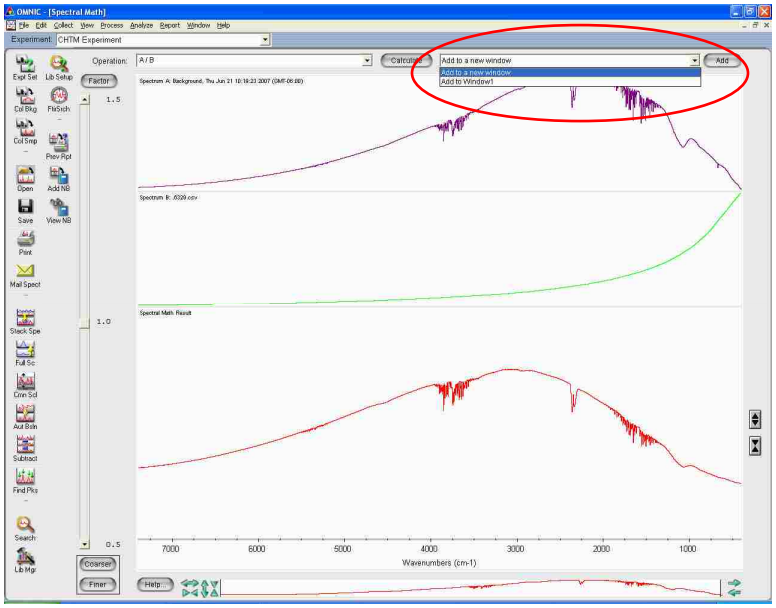

Figure App. B. 9

16. Save the new corrected background.

17. In the **Experiment Setup** window under the Collect tab in the Background Handling part select Use specified background file: and click Browse to find and select the corrected background that was saved in Step 16. Then change the Final Format to **% Transmittance** so that each collected sample will be automatically divided by the corrected background.

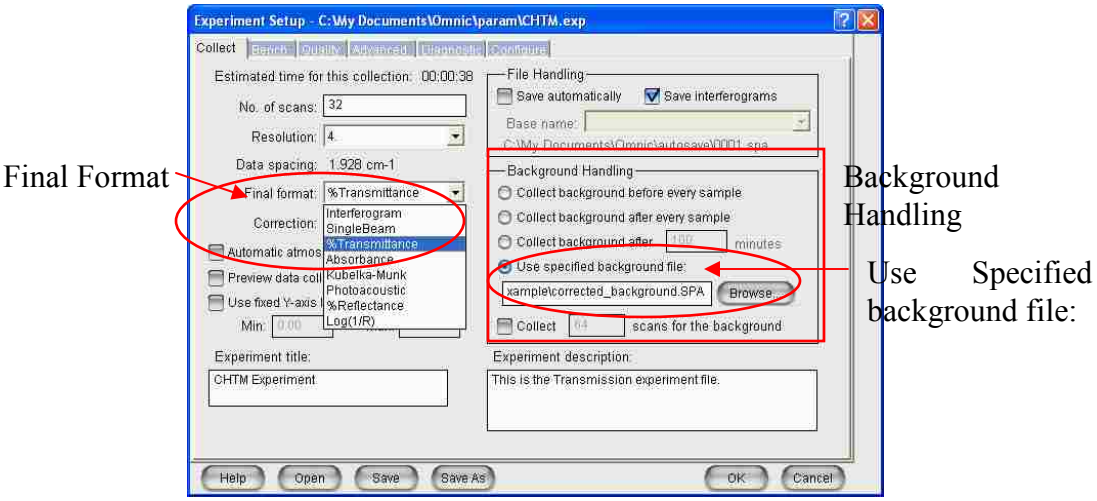

Figure App. B. 10

Appendix B

Part 2 Example

1. Collect Background.

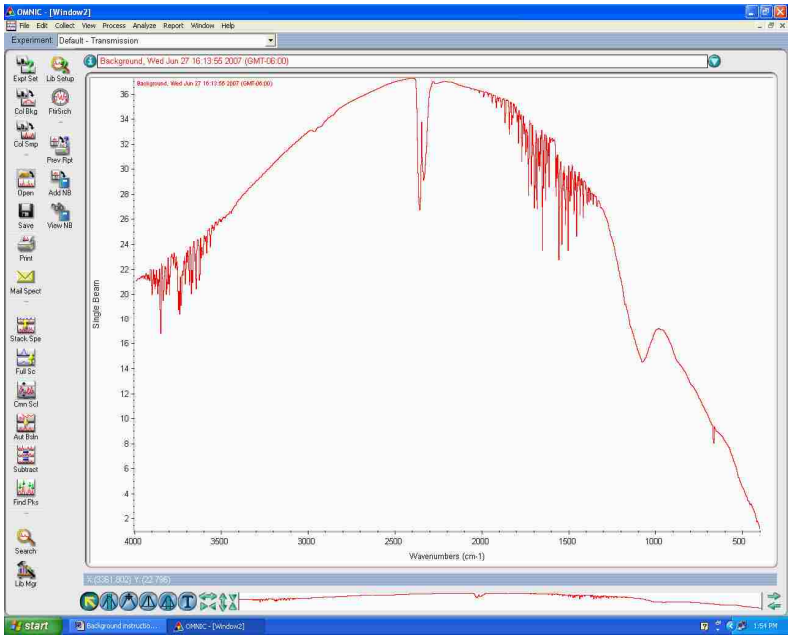

Figure App. B. 11

2. Open Velocity Correction Curve. C:\My Documents\OMNIC\Spectra\Velocity Correction Curves. The spectra file is the default save/open file when OMNIC is started. Change Y units to Single Beam and Resolution to match the background spectrum.

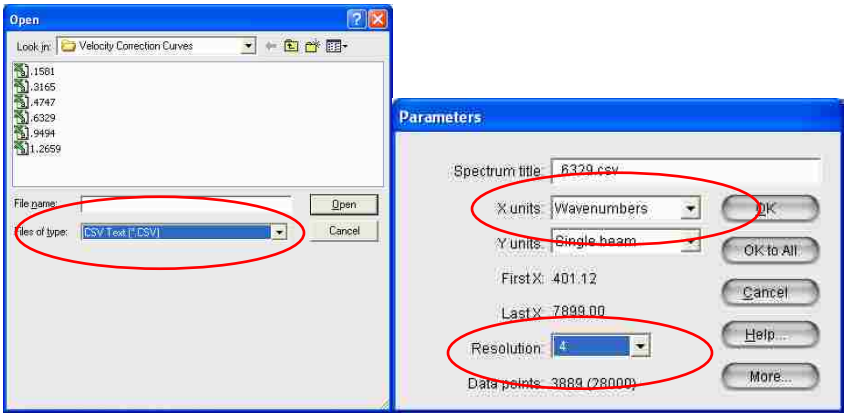

Figure App. B. 12

3. Use spectral math to divide Background by Correction Curve.

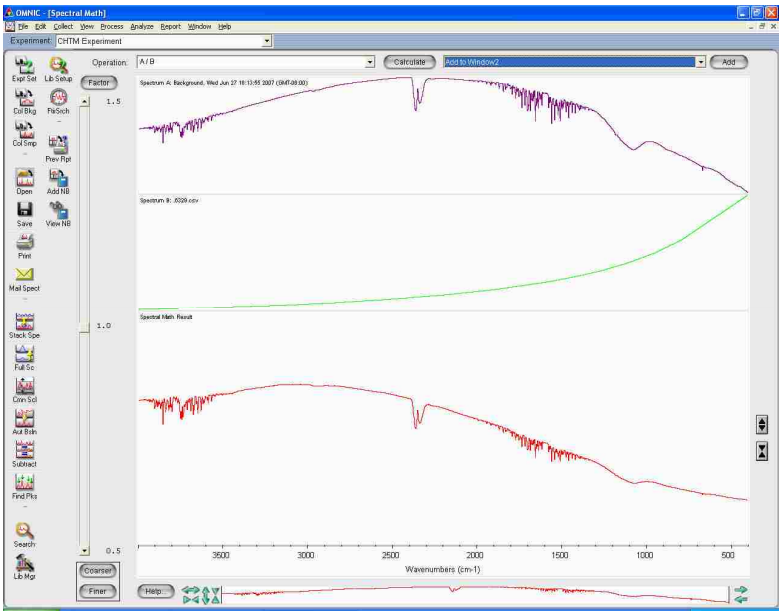

Figure App. B. 13

4. Save corrected background.

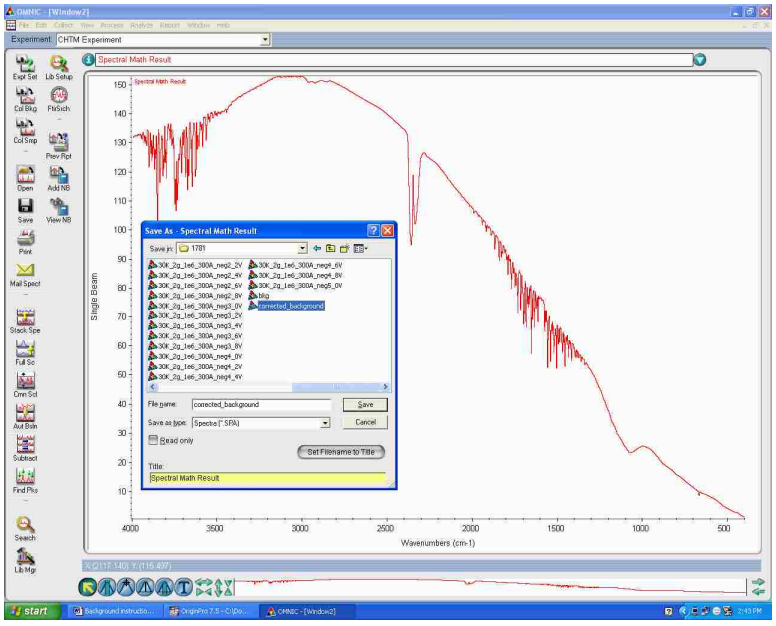

Figure App. B. 14

5. Use Specified background and change Final format to % Transmittance.

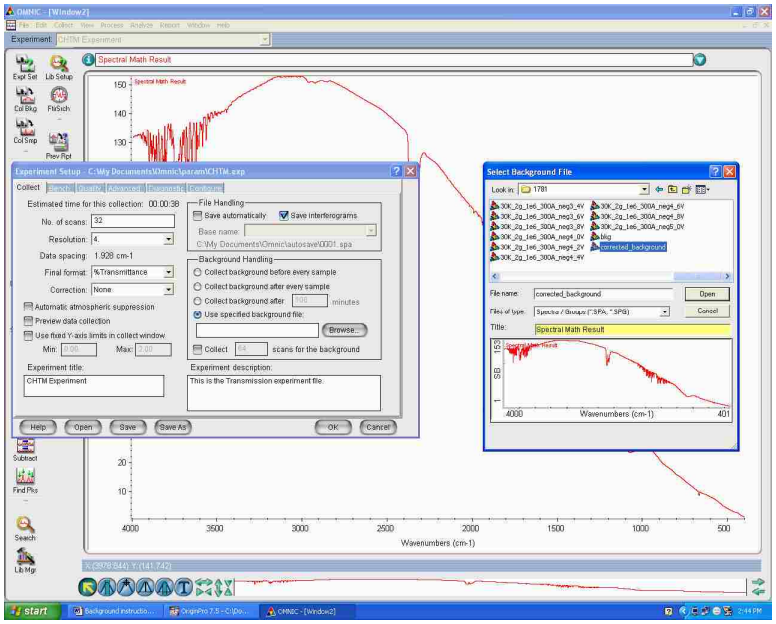

Figure App. B. 15

6. Collect and save samples

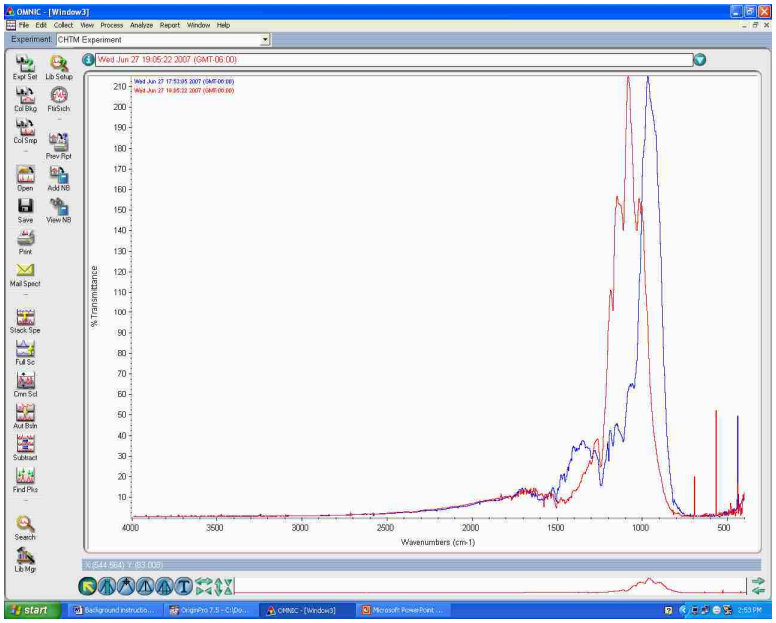

Figure App. B. 16

References

[1] http://en.wikipedia.org/wiki/Image:EM_spectrum.svg

[2] Planck, Max. On the Law of Distribution of Energy in the Normal Spectrum. *Annalen der Physik* vol. 4, p. 553, 1901.

[3] Vincent, John David. *Fundamentals of Infrared Detector Operation and Testing*. John Wiley & Sons, New York, 1990.

[4] Dereniak, E. L., G. D. Boreman. *Infrared Detectors and Systems*. John Wiley and Sons, New York, 1996.

[5] http://upload.wikimedia.org/wikipedia/en/5/5b/Atmospheric_transmittance_infrared.gif

[6] Rogalski, A. *Quantum well photodetectors in infrared detector technology*. J. Appl. Phys., Vol. 93, No. 8, 15 April 2003.

[7] Jones, R. Clark. Performance of Detectors for Visible and Infrared Radiation," *Advances in Electronics*, Vol. 5, Academic Press, New York (1953).

[8] http://www.infratec.de/en/infratec.html

[9] Rogalski, A. Infrared detectors: status and trends, Progess in Quantum Electronics **27** 66 (2003)

[10] Lawson, W. D., S. Nielson, E. H. Putley, and A. S. Young, Preparation and properties of HgTe-CdTe, J. Phys. Chem. Solids **9**, 325-329 (1959).

[11] Rogalski, A. *Infrared Detectors*. Gordon and Breach Science Publishers 2000

[12] Tribolet, P., S. Blondel, P. Costa, A. Combette, G. Destefanis, P. Ballet, J.-P. Zanatta, O. Gravrand, C. Langeron, J.-P. Chamonal and A. Million. MWIR focal plane arrays made with HgCdTe grown by MBE on germanium substrates. SPIE, 2006

[13] Gunapala, S.D., S.V. Bandara, J.K. Liu, C.J. Hill, S.B. Rafol, J.M. Mumolo, J.T. Trinh, M.Z. Tidrow, P.D. LeVan. 1024 x 1024 pixel mid-wavelength and long-wavelength infrared QWIP focal plane arrays for imaging applications. Semicond. Sci. Technol. **20** No. 5 (2005)

[14] Smith, D.L. and C. Mailhiot. Proposal for strained type II superlattice detectors, J. Appl. Phys. **62**, (6), 2545-2548 (1987)

[15] Sai-Halasz, G. A., R. Tsu, L. Esaki. A new semiconductor superlattice, Appl. Phys. Lett. **30**, (12), 651-653 (1977)

[16] Esaki, L. *Proceedings of the 17th International Conference on the Physics of Semiconductors*, edited by J.D. Chadi, and W.A. Harrison (Springer, New York), p. 473 1985

[17] Smith, D.L. and C. Mailhiot. **k·p** theory of semiconductor superlattice electronic structure. I. Formal results, Phys. Rev. B **33**, No. 12 8345-8359 1986

[18] Mailhiot, C., and D.L. Smith. **k·p** theory of semiconductor superlattice electronic structure. II. Application to $Ga_{1-x}In_xAs$-$Al_{1-y}In_yAs$ [100] superlattices Phys. Rev. B **33**, No. 12 8360-8372 1986

[19] Dente, G.C., and M.L. Tilton. Pseudopotential methods for superlattices: Applications to mid-infrared semiconductor lasers, J. Appl. Phys. **86**, No. 3, 1420-1429 1999

[20] Dente, G.C., and M.L. Tilton. Comparing pseudopotential predictions for InAs/GaSb superlattices, Phys. Rev. B **66**, 165307 (2002)

[21] Wei, Y. and M. Razeghi. Modeling of type-II InAs/GaSb superlattices using an empirical tight-binding method and interface engineering, Phys. Rev. B **69**, 085316 (2004)

[22] Rogalski, A. Competitive technologies of third generation infrared photon detectors, Opto-Electron. Rev., **14**, no. 1, 87-101, 2006

[23] Youngdale, E. R., J. R. Meyer, C. A. Hoffman, F. J. Bartoli. Auger lifetime enhancement in InAs-$Ga_{1-x}In_xSb$ superlattices, Appl. Phys. Lett. **64**, 3160, 1994

[24] Bürkle, L., and F. Fuchs. InAs/(GaIn)Sb superlattices: a promising material system for infrared detection, *Handbook of Infrared Detection and Technoligies*, Elsevier, Oxford, 2002

[25] Rehm, R., M. Walther, J. Schmitz, J. Fleibner, F. Fuchs, W. Cabanski and J. Ziegler. InAs/(GaIn)Sb short period superlattices for focal plane arrays, Proc. of SPIE Vol. 5783, 123-130, 2006

[26] Rehm, R., M. Walther, J. Schmitz, J. Fleibner, S. Kopta, F. Fuchs, W. Cabanski and J. Ziegler. Growth of InAs/GaSb short-period superlattices for high-resolution mid-wavelength infrared focal plane array detectors, J. Crys. Grow. **278**, 1560161, 2005

[27] Yau, H., Y. Wei, M.Z. Tidrow, V. Yazdanpanah, M. Razeghi and V. Nathan. Uncooled operation of type-II InAs/GaSb superlattice photodiodes in the mid-wavelength infrared range, Appl. Phys. Lett. **86** 233106-233109, 2005

[28] Yau, H., Y. Wei, A. Hood, M.Z. Tidrow, V. Yazdanpanah, M. Razeghi and V. Nathan. High-performance type-II InAs/GaSb superlattice photodiodes with cutoff wavelength around 7 μm. Appl. Phys. Lett., **86**, 091109-091112, 2005

[29] Bergman, J., G.J. Sullivan, A. Ikhlassi, C. Grein, R.E. DeWames, J.R. Waldrop, H. Yang, M. Flatte, K. Mahalingam, M. Zhong, M. Weimer. Molecular beam epitaxy growth of high quantum effiency InAs/GaSb superlattice detectors, J. Vac. Sci. Technol. B, **23**, no. 3 1144-1148 (2005)

[30] Nguyen, B.-M., D. Hoffman, Y. Wei, P.-Y. Delaunay, A. Hood and M. Razeghi. Very high quantum efficiency in type-II InAs/GaSb superlattice photodiode with cutoff of 12 μm, Appl. Phys. Lett. **90**, 231108 (2007)

[31] Aifer, E.H., J.G. Tischler, J.H. Warner, I. Vurgaftman, W. W. Bewley, J.R. Meyer, J.C. Kim, L.J. Whitman, C.L. Canedy, and E.M. Jackson. W-structured type-II superlattice long-wave infrared photodiodes with high quantum efficiency, Appl. Phys. Lett. **89**, 053519 (2006)

[32] B.-M. Nguyen, D. Hoffman, P.-Y. Delaunay and M. Razeghi. Dark Current suppression in type II InAs/GaSb superlattice long wavelength infrared photodiodes with M-structure barrier, Appl. Phys. Lett. **91**, 163511 (2007)

[33] B.-M. Nguyen, D. Hoffman, P.-Y. Delaunay, M. Razeghi and V. Nathan. Polarity inversion of type-II InAs/GaSb superlattice photodiodes, Appl. Phys. Lett. **91**, 103503 (2007)

[34] Rodriguez, J.B., E. Plis, G. Bishop, Y.D. Sharma, H. Kim, L.R. Dawson, and S. Krishna. nBn structure based on InAs/GaSb type-II strained layer superlattices, Appl. Phys. Lett. **91**, 043514 (2007)

[35] E. H. Aifer, J. G. Tischler, J. H. Warner, I. Vurgaftman, J. R. Meyer, C. L. Canedy, and E. M. Jackson. Dual band LWIR/VLWIR type-II superlattice photodiodes, SPIE, v**5783**, 112–122 (2005)

[36] Khoshakhlagh, A., J. B. Rodriguez, E. Plis, G. D. Bishop, Y. D. Sharma, H. S. Kim, L. R. Dawson and S. Krishna. Bias dependent dual band response from InAs/Ga(In)Sb type II strain layer superlattice detectors, Appl. Phys. Lett. **91**, 263504, (2007)

[37] Maimon, S. and G.W. Wicks. nBn detector, an infrared detector with reduced dark current and higher operating temperature, Appl. Phys. Lett. **89**, 151109 (2006)

[38] Rogalski, A. Infrared Phys. **28**, 139 (1988)

[39] Plis, E., S. Annamalai, K.T. Posani, S. Krishna, R.A. Rupani, and S. Ghosh. Midwave infrared type-II InAs/GaSb superlattice detectors with mixed interfaces, J. Appl. Phys. **100**, 014510 (2006)

[40] Hill, C. J., J. V. Li, J. M. Mumolo, S. D. Gunapala. MBE grown type-II MWIR and LWIR superlattice photodiodes, Infrared Phys. and Tech. **50** v-vii, 189 (2007)

[41] Little, J.W., S.P. Svensson, W.A. Beck, A.C. Goldberg, S.W. Kennerly, T. Hongsmatip, M. Winn and P. Uppal. Thin active region, type II superlattice photodiode arrays: Single-pixel and focal plane array characterization, J. Appl. Phys. **101**, 044514 (2007)

[42] Gin. A., Y. Wei, J. Bae, A. Hood, J. Nah and M. Razeghi. Passivation of Type II InAs/GaSb superlattice photodiodes, Thin Solid Films, (447-448):489-492, (2004)

[43] Hood, A., P.-Y. Delaunay, D. Hoffman, B.-M. Nguyen, Y. Wei, M. Razeghi and V. Nathan. Near bulk-limited R_0A of long-wavelength infrared type-II InAs/GaSb superlattice photodiodes with polyimide surface passivation, Appl. Phys. Lett., **90**, 233513 (2007)

[44] Rehm, R. M. Walther, F. Fuchs, J. Schmitz and J. Fleissner. Passivation of InAs/(GaIn)Sb short-period superlattice photodiodes with 10 μm cutoff wavelength by epitaxial overgrowth with $Al_xGa_{1-x}As_ySb_{1-y}$, Appl. Phys. Lett. **86**, 173501 (2005)

[45] Plis. E., J.-B. Rodriguez, S. J. Lee and S. Krishna. Electrochemical sulphur passivation of InAs/GaSb strain layer superlattice detectors, Electron. Lett. **42**, 21 (2006)

[46] Gin, A., Y. Wei, A. Hood, A. Bajowala, V. Yazdanpanah, M. Razeghi and M. Tidrow. Ammonium sulfide passivation of Type-II InAs/GaSb superlattice photodiodes, Appl. Phys. Lett. **84**, No. 12 2037 (2004)

[47] Vogt, A., A. Simon, H. L. Hartnagel, J. Schikora, V. Buschmann, M. Rodewald, H. Fuess, S. Facsko, C. Koerdt and H. Kurz. Ohmic contact formation mechanism of the PdGeAu system on n-type GaSb grown by molecular beam epitaxy, J. Appl. Phys. **83**, No. 12, 7715-7719 (1998)

[48] Chandrasekhar Rao, T. V., J. Antoszewski, L. Faraone, J. B. Rodriguez, E. Plis and S. Krishna. Characterization of carriers in GaSb/InAs superlattice grown on conductive GaSb substrate, Appl. Phys. Lett. **92**, 012121 (2008)

[49] Rehm, R., M. Walther, J. Fleibner, J. Schmitz, J. Ziegler, W. Cabanski and R. Breiter. Bispectral Thermal Imaging with Quantum Well Infrared Photodetectors and InAs/GaSb Type-II Superlattices, Proc. of SPIE, Vol. 6206, (2006)